Molecular insights into substrate translocation in an elevator-type metal transporter

Yao Zhang[1,*], Majid Jafari[1,*], Tuo Zhang[1,2,*], Dexin Sui[1], Luca Sagresti[3,4], Kenneth M. Merz, Jr.[1,5,#], Jian Hu[1,5,#]

[1]Department of Biochemistry & Molecular Biology, Michigan State University, MI 48824

[2]College of Food Science and Nutritional Engineering, China Agricultural University, Beijing, 100083, China

[3]Scuola Normale Superiore, Piazza dei Cavalieri 7, I-56126 Pisa, Italy and CSGI

[4]Istituto Nazionale di Fisica Nucleare (INFN) sezione di Pisa, Largo Bruno Pontecorvo 3, 56127 Pisa, Italy

[5]Department of Chemistry, Michigan State University, MI 48824

[*] These authors equally contributed to this work.

[#] To whom correspondence should be addressed: Jian Hu, hujian1@msu.edu; Kenneth M. Merz, Jr, merz@chemistry.msu.edu

Summary

The Zrt/Irt-like protein (ZIP) metal transporters are key players in maintaining the homeostasis of a panel of essential microelements. The prototypical ZIP from *Bordetella bronchiseptica* (BbZIP) is an elevator transporter, but how the metal substrate moves along the transport pathway and how the transporter changes conformation to allow alternating access remain to be elucidated. Here, we combined structural, biochemical, and computational approaches to investigate the process of metal substrate translocation along with the global structural rearrangement. Our study revealed an upward hinge motion of the transport domain in a high-resolution crystal structure of a cross-linked variant, elucidated the mechanisms of metal release from the transport site into the cytoplasm and activity regulation by a cytoplasmic metal-binding loop, and unraveled an unusual elevator mode in enhanced sampling simulations that distinguishes BbZIP from other elevator transporters. This work provides important insights into the metal transport mechanism of the ZIP family.

Key Words

Transporter, Zinc, ZIP, Structure, Transport mechanism, Molecular dynamics simulation, Metadynamics

Introduction

A panel of first-row *d*-block metal elements are essential for life. Among the transporters that control the fluxes of these micronutrients across biological membranes, the Zrt/Irt-like protein (ZIP) family plays a central role[1-3]. The ZIP family consists of divalent metal transporters that are ubiquitously expressed in all kingdoms of life, mediating metal flux into the cytoplasm from the extracellular milieu or from the intracellular organelles/vesicles. In humans, the fourteen ZIPs (ZIP1-14) are involved in zinc, iron, or manganese homeostasis. Some ZIPs are associated with human diseases[4-9] and are therefore considered as potential targets for novel therapies[10-18]. For instance, ZIP6 is tightly associated with cancer cell growth and proliferation[12,19-21], and a monoclonal antibody against human ZIP6 is being tested in clinical trials for breast cancer and other solid tumors[22,23]. ZIP4, which was found to be aberrantly upregulated in many cancers, has been shown to be associated with cancer cell growth and metastasis[24-32], whereas the ER-residing ZIP7 is essential for B cell development[33] and a druggable node in the Notch pathway[17].

Recent structural studies have begun to elucidate the transport mechanism of ZIPs. The structure of a prototypic ZIP from *Bordetella bronchiseptica* (BbZIP) revealed the structural framework of the conserved transmembrane domain that is composed of eight transmembrane helices (TM) and two tethered metal binding sites (M1 and M2) at the transport site[34]. More BbZIP structures in the inward-facing conformation (IFC) were later solved by x-ray crystallography and cryo-electron microscopy (cryo-EM)[34-38]. An elevator transport mode has been proposed based on the two-domain architecture, evidence from evolutionary covariance, and an experimentally validated outward-facing conformation (OFC) model generated by repeat-swap homology modeling[36,38]. According to the proposed mechanism, a TM bundle composed of TM1/4/5/6 (the transport domain), carrying the metal substrate(s), moves vertically relative to the static scaffold domain composed of TM2/3/7/8 to achieve alternating access. The structure models predicted by AlphaFold2 suggested that the elevator mode is commonly used by the ZIPs from different subfamilies[38,39]. Due to the lack of structural similarity to other well-characterized elevator transporters[40], a recent structural survey did not consider BbZIP to be a classical elevator transporter, suggesting that the mechanism may be fundamentally different from what has been established for elevator transporters. Therefore, it is imperative to elucidate the detailed processes of conformational change and translocation of metal substrate through the transporter.

In this work, we integrated structural, biochemical, and computational approaches to address these critical questions. A high-resolution crystal structure of an Hg^{2+}-crosslinked BbZIP variant revealed an upward hinge motion of the transport domain and identified a third metal binding site at the end of the transport pathway. Structural analysis and functional studies allowed us to propose mechanisms for metal release from the transport site into the cytoplasm and for activity regulation via a cytoplasmic loop containing the third metal binding site. Our enhanced sampling simulations not only supported these proposed mechanisms but also captured for the first time the process of the elevator motion. The combined experimental and computational data revealed an unprecedented mode of transport for elevator transporters.

Results

An upward hinge motion of the transport domain revealed in the structure of a crosslinked transporter

Our previous study has suggested that when the transport domain moves upward against the scaffold domain to switch from the IFC to the OFC, the distances between some residue pairs in the IFC become shorter in the OFC[38], such as A95 and A214 on the scaffold and transport domains, respectively (**Figure 1A**). This represents the dynamics of the transporter, which is essential for the alternating access mechanism, but it also poses a challenge for structural studies. To fix the relative orientation of the two domains for structural characterization, A95 and A214 were substituted by cysteine residues, allowing chemical cross-linking between them as there is no endogenous cysteine residue in BbZIP. To promote disulfide bond formation, the membrane fraction of the *E.coli* cells expressing the A95C/A214C variant was treated with [Cu(II)(1,10-phenanthroline)$_3$] complex at room temperature and then applied to Western blot to detect the crosslinked species. As shown in **Figure 1B**, the treatment led to the generation of a new band with reduced migration in the non-reducing SDS-PAGE, which was eliminated upon the addition of a reducing agent 2-mercaptoethanol. The same treatment of wild-type BbZIP, A95C, or A214C single variants did not result in band shift, indicating that a disulfide bond has been formed between C95 and C214. Given that the Cα distance between A95 and A214 (10.1 Å) in the IFC, as shown in the cadmium (Cd) bound structure (PDB: 5TSB, **Figure 1A**), is longer than that between two disulfide bonded cysteine residues (3.0-7.5 Å[41]), the formation of the C95-C214 disulfide bond is consistent with the proposed elevator transport mode[36,38]. The inability to completely convert the A95C/A214C variant to the cross-linked form, presumably due to the highly dynamic nature of the transporter, led us to use mercury (Hg) as a cross-linker for structural study. As shown in **Figure 1C**, addition of $HgCl_2$ to the purified A95C/A214C variant caused a clear band shift in the non-reducing SDS-PAGE only for the double variant but not for any of the single variants (C95 or C214). The band shift was prevented by the pretreatment of the purified protein with N-ethylmaleimide (NEM), a thiol reacting agent, and completely abolished by 2-mercaptoethanol, supporting that the two introduced cysteine residues have been cross-linked by Hg^{2+}.

After a brief treatment with EDTA and desalting, the Hg^{2+}-cross-linked sample was crystallized in lipidic cubic phase under a Cd-free condition, yielding a structure of BbZIP in a new IFC conformation at 1.95 Å, the highest resolution for BbZIP to date (**Figure 1D**, **Table S1**). Similar to the structures of BbZIP in the apo state[36,38], the new structure showed nine TMs with the N-terminal TM0 only weakly associated with TM3 and TM6. As expected, a Hg^{2+} is chelated by C95 from TM2 and C214 from TM5 (**Figures 1D** & **S1**), locking the relative orientation between the transport and scaffold domains. When compared with the previously solved structure of BbZIP in the Cd-bound state (PDB: 5TSB), the new structure revealed an upward rotation of the transport domain relative to the scaffold domain (**Figures 1E & S2**), which is contrast to the structures in the metal-free state that consistently showed a rotation of the transport domain in the opposite direction[36,38]. Of great interest, when the scaffold domains of the representative IFC structures, including the new structure, are aligned, a continuous rigid-body hinge motion of the transport domain can be visualized (**Figure 1E**), which was recapitulated in the computational simulations shown in later sections.

Characterization of the high-affinity metal binding sites

Although the cross-linked A95C/A214C variant was briefly treated with EDTA and crystallized in a Cd^{2+}-free buffer, the two tethered metal binding sites (M1 and M2) are still occupied by Cd^{2+} (**Figure 2A**). The coordination spheres of the bound Cd^{2+} are not significantly affected by the rigid-body hinge motion of the transport domain, but a chloride ion (Cl^-) was found to coordinate

with Cd^{2+} at the M1 site (**Figure S3)**. As there is no evidence to support metal co-transport with Cl^- and there are no residues that interact with Cl^- directly, it is unlikely that Cl^- is a substrate of BbZIP. Rather, the anion may assist metal release from the high-affinity transport site by neutralizing the charges on the cation and excluding the otherwise coordinating sulfur atom of M99 from the coordination sphere (**Figure 2A**). In the new structure, a third metal binding site (M3) was identified at the end of the metal release tunnel. The Cd^{2+} bound at the M3 site, with an occupancy of 0.84, is coordinated with two histidine residues (H149 and H151) from the intracellular loop 2 (hereafter IL2), D144 from TM3, E276 from TM7, and an ordered water molecule, forming a distorted octahedral coordination sphere (**Figures 2B** & **S4**). Recently, a cryo-EM structure of wild-type BbZIP showed a similar M3 binding site[37], and structural comparison of the two structures revealed some minor differences (**Figure S2C**), which is consistent with a flexible IL2 and dynamic metal binding at the M3 site. To examine whether M1-M3 are an authentic metal binding sites in solution, wild-type BbZIP and the H149A/H151A variant with the eliminated M3 site purified in the presence of 0.25 mM Cd^{2+} were applied to a size-exclusion chromatography column equilibrated with a Cd-free solution, and the peak fractions were analyzed by using inductively coupled plasma mass spectrometry (ICP-MS) to quantify the bound metal. The determined Cd/BbZIP molar ratio was 3.0±0.3 and 1.8±0.3 (mean±s.e.m., n=2, **Figure 2C**) for wild-type protein and the H149A/H151A variant, respectively, indicating that Cd^{2+} is indeed bound at the M3 site in solution. Although the IL2 of BbZIP was found to be severely disordered in the previous crystal structures, Cd^{2+} binding to the M3 site stabilizes the IL2 which folds into two short anti-parallel β-strands and forms hydrogen bonds with the rest of the protein. The large B-factor of the Cd^{2+}-stabilized IL2 is consistent with the notion that it is intrinsically disordered (**Figure S5**). As a result, the metal release tunnel in the new structure, starting from the M1 site, is divided into two parallel pathways – one is connected to the M3 site (Path 1), whereas the other, filled with water molecules, is directly connected to the cytoplasm (Path 2) (**Figure 2D**).

A conserved metal release mechanism

To understand the function of the M3 site, we studied the residues in human ZIP4 (hZIP4) that are topologically equivalent to those forming the M3 site in BbZIP (**Figure 2E**). It is known that most ZIPs have a histidine-rich segment in the IL2[2,3], and D144 and E276 are generally conserved in ZIPs from different subfamilies and different species (**Figure S6**). E417 in hZIP4, which is equivalent to D144 in BbZIP, was found to be dispensable for activity (**Figure 2F**) as the E417A variant exhibited a modestly increased V_{max} when compared to wild-type hZIP4. Different from the short IL2 of BbZIP, the corresponding loop of hZIP4 is longer and harbors a his-rich cluster containing five histidine residues. We replaced all the histidine residues with alanine to generate the 5HA variant which exhibited a drastically changed transport kinetics (**Figure 2G**). The dose-dependent profile appeared to be linear at low zinc concentrations and slightly bent only at high zinc concentrations. Because the curve did not saturate in the range of zinc concentrations tested in this work, we could not fit the curve to obtain the values for K_M and V_{max}, but the curve profile suggested that both K_M and V_{max} increased. The results of the variants of E417A and 5HA suggested that the residues corresponding to those forming the M3 site in BbZIP appear to negatively regulate the activity of hZIP4. Consistently, replacing H149 and H151 with alanine led to an increased activity of BbZIP[37]. Unexpectedly, D604 in hZIP4, which is equivalent to E276 in the M3 site, is indispensable for the transport activity. Substitution of D604 with alanine completely abolished the zinc transport activity (**Figure 2H**), and only the D604E variant, but not the D604H variant, preserved an activity similar to that of wild-type hZIP4

(**Figure 2I**). Notably, E276 in human ZIP2, the D604-equivalent residue, was also shown to be absolutely essential for the transport activity[42].

To understand the role of E276 in BbZIP and the equivalent residues in other ZIPs, multiple metal bound structures of BbZIP (PDB: 5TSA and 7Z6M, and the Hg^{2+}-cross-linked structure) were superimposed, revealing potential metal release pathways from the transport site to the cytoplasm where E276 plays a role in the metal relay (**Figure 2K**). Since the M2 site has no direct access to the cytoplasm (blocked by I174 and V215, **Figure 2D**)[35], metal release from the transport site likely starts from the M1 site. Swinging of the side chain of H177 away from the M1 site opens a door for metal to leave the high-affinity transport site. Joining the flipped H177, E276 forms a transient metal binding site and then undergoes a nearly right-angle rotation to direct the metal substrate to the M3 site (Path 1) where the metal is retained before being released into the cytoplasm. Therefore, E276 appears to play multiple roles in the process of metal release from the transport site to the cytoplasm. First, it transiently holds the metal that leaves the M1 site with the flipped H177. This role has been suggested by our and other previous studies[34,36,37]. Second, its structural flexibility, likely due to P279, which is present in many ZIPs (**Figure S6**), and the high dynamics of the segment connecting TM7 and TM8 (**Figure S5**), allows it to direct the metal to the M3 site. Indeed, replacing P607 in hZIP4 (equivalent to P279 in BbZIP) with alanine reduced the transport activity by ~60% (**Figure 2J**). Third, it contributes to metal binding to the M3 site. As a high-affinity metal binding site (**Figure 2C**) that is within the transport pathway and negatively regulates the metal transport activity (**Figures 2F** & **2G**), the M3 site can be described as a metal sink in addition to the proposed autoinhibitory site that acts only upon zinc overload[37]. As Path 2 is filled with water (**Figure 2D**), can it be used as an alternative pathway for metal release to the cytoplasm when Path 1 is blocked by the occupied M3 site? We investigated this important question using computational approaches.

Metal release pathways and elevator motion revealed by metadynamics simulations

Next, we deployed enhanced sampling simulations, i.e. metadynamics (MTD) simulations in this work, to study the process of metal release from the transport site into the cytoplasm. MTD simulations have been used to study substrate binding and release in various transporters[43-46], but have not been applied to any highly charged system like BbZIP due to the challenges in simulating the behaviors of transition metals. Established on our recent work on zinc binding to various ligands[47,48], we systematically identified the optimal configuration of parameters governing the system dynamics and addressed the pressing issue of zinc translocation through BbZIP by using volumetric collective variables (CVs) and iteratively optimizing the MTD simulation parameters.

The cryo-EM structure of wild-type BbZIP (PDB: 8GHT) was used as the initial structural model in the MTD simulations because it is the only experimentally solved structure of a BbZIP dimer[37], of which the dimerization interface has been validated by chemical crosslinking[38]. The cryo-EM structure of the BbZIP is highly superimposable on the crystal structure of BbZIP in the Cd-bound state (PDB: 5TSB) (**Figure S7A**). To generate the initial structural model for simulations, Cd^{2+} ions at the M1-M3 sites in the cryo-EM structure were replaced by Zn^{2+}, which did not lead to significant structural changes after reaching equilibrium (**Figure S7B**). When standard molecular dynamics (MD) simulations were performed on the Zn-bound structural model for up to 2 μs, no significant structural change or metal movement was noticed, indicating that the Zn-bound state represents a stable conformation and also necessitating the use of MTD

simulations to accelerate the process through enhanced sampling. In MTD simulations, a biasing potential was applied to the zinc ion bound at the M1 site because the M1 site has been shown to be the authentic transport site[35].

Given that the process of metal release may be affected by the folding state of the IL2 (**Figure 2D**) and the metal binding states of the transporter, we conducted simulations in the following four scenarios. In the first scenario, the M1 and M2 sites were occupied by Zn^{2+} but the IL2 was unfolded with no Zn^{2+} bound at the M3 site, mimicking the conformational states shown in the Cd-bound crystal structures (PDB: 5TSB and 7Z6M). To unfold the IL2, a steered MD simulation was conducted to generate the initial model. In the second scenario, the M1-M3 sites were occupied by Zn^{2+} and the IL2 was in the folded state, mimicking the conformational state solved in the cryo-EM structure (PDB: 8GHT) and the new structure reported in this work. In the third scenario, the M1 and M2 sites were occupied by Zn^{2+} and the IL2 was in the folded state with a pre-formed but empty M3 site to test the accessibility of metal to an unoccupied M3 site upon a folded IL2. In the last scenario, the settings are the same as in the second scenario except that the metal at the M2 site was removed to study the role of the metal bound at the M2 site in metal release. The settings and results of all MTD simulations are summarized in **Table S2**.

In the first scenario, three independent runs of MTD simulations revealed multiple neighboring local minima in the free energy surface maps (**Figures 3A** & **S8A**), which allowed us to construct a pathway for metal release from the M1 site to the cytoplasm (**Figure 3B**). It starts with the flip of the H177 side chain away from the M1 site, as observed in our early computational work[49], and the metal is then coordinated by both H177 and E276 at the transient Zn^{2+} binding site, followed by its movement to the M3 site. Of great interest, this process is essentially in agreement with the proposed Path 1 based on the experimentally solved structures (**Figure 2K**). A notable difference is that Zn^{2+} at the M3 site was coordinated with only three residues (D144 plus two of H149, H177, H275, and E276) while H151 in the IL2 did not join the M3 site in any simulation. Although it is possible that the folding of the 18-residue IL2 takes a longer time than the simulation length to allow H151 to join the M3 site, another possibility that H151 really does not participate in metal binding during the metal release process cannot be excluded. Nevertheless, our MTD simulations indicated that (1) E276 is directly involved in the processes of metal release from the M1 site and metal delivery to the M3 site; and (2) the metal from the transport site can be retained at the M3 site in its journey to the cytoplasm as the M3 site is a significant local minimum in the free energy surface map.

In the second scenario, four out of five simulations showed that Zn^{2+} remained at the M1 site until the biasing potential pushed it out of the high-affinity binding site before it was finally released into the cytoplasm (**Table S2**). Since the IL2 was in the folded state and the M3 site was occupied throughout the simulations, the metal from the M1 site passed through Path 2 to reach the cytoplasm (**Figures 2D** & **2K**). However, this occurred only when the conformational changes of the portions of TM4 and TM5 on the cytoplasmic side and the IL2 took place to create a larger space for the metal to pass through (**Figures 3C & S8B**). Considering the requirement for a significant structural rearrangement of multiple structural elements, metal passing through Path 2 is likely to be kinetically unfavorable compared to Path 1. This result is consistent with the suggested role of the M3 site as an autoinhibitory zinc sensor that abolishes the zinc transport activity when the M3 site is occupied upon intracellular zinc overload[37].

Unexpectedly, for one simulation in the second scenario, Zn^{2+} at the M1 site was found to move backward and eventually released into the periplasm. The RMSF analysis showed that the

residues in the transport domain exhibit greater structural fluctuation than those observed in the first scenario (**Figure S9**), whereas the intracellular loops, including the IL2, showed smaller structural fluctuation due to the folded and stabilized IL2. Close inspection of the conformational change revealed that TM4 and TM5, and especially the latter, underwent a significant upward movement relative to the scaffold domain, along with a swing of the portion of TM5 on the periplasmic side away from the tunnel (**Figures 4A** & **4B**), opening a path for the metal to be released from the M1 site into the periplasm. Concomitantly, the portion of TM5 on the cytoplasmic side moved toward the tunnel to narrow the pathway toward the cytoplasm (**Figure 4A**). This large structural rearrangement of TM4 and TM5 and the rotation of TM1 and TM6 (**Figure 4C**) resulted in an OFC-like conformation with the transport site lifted by ~6 Å toward the periplasm, which is a hallmark of elevator transporters, allowing the metal to be released into the periplasm when this major conformational change took place. Analysis of the changes in distance between the residues within and between the transport and scaffold domains provided further support for the proposed elevator motion. For instance, the Cα distance between A95 (TM2) on the scaffold domain and A214 (TM5) on the transport domain changed from ~9 Å to ~5 Å when the major conformational change occurred (at ~180 ns as indicated in **Figure 4D**), which is short enough to allow the disulfide bond formation for the A95C/A214C variant (**Figure 1B**). Similarly, the distance between S106 (TM2) on the scaffold domain and I196 (TM5) on the transport domain also increased at ~180 ns, indicative of the vertical movement and the outward swing of the periplasmic side of TM5 during the conformational transition (**Figure 4D**). In contrast, the distances between the residues within the transport domain (A71 on TM1 and V234 on TM6) or the scaffold domain (S106 on TM2 and M301 on TM8) varied within a narrow range during the simulations (**Figure 4D**). The large vertical displacement between the transport and scaffold domains and the much smaller structural fluctuations within each domain indicate a rigid-body motion of the transport domain, which is another hallmark of elevator transporters. Of great interest, the overall conformational change leading to the OFC-like state is essentially a combination of an extrapolation of the hinge motion revealed by the experimentally solved IFC structures (**Figure 1E**) and a vertical sliding for the transport domain (**Figure 4E**). To the best of our knowledge, such a conformational change has not been observed in other elevator transporters[40,50,51].

Three runs of MTD simulations in the third scenario showed that the M3 site remained empty while the IL2 was in the folded state, indicating that the metal from the M1 site has no direct access to the pre-formed but unoccupied M3 site. This result suggests that, in order to form the state with an occupied M3 site and a fully folded IL2, as observed in the experimentally solved structures, metal binding to the M3 site should precede the folding of the IL2. As Path 1 is blocked under this condition, Zn^{2+} at the M1 site was found to be either released into the cytoplasm via Path 2 or remained near the M1 site (**Table S2**). In one simulation, however, the metal was released into the periplasm when the transport domain underwent a combined hinge motion and vertical sliding, as observed in the second scenario (**Figure S10A**).

In the last scenario, we tested the role of the M2 site in the process of metal release from the M1 site. The M2 site is present in most ZIPs but disruption of the M2 site only modestly reduced the zinc transport activity[35]. Only one of five runs of MTD simulations with an unoccupied M2 site showed that the metal from the M1 site was released into the cytoplasm (**Table S2**), in sharp contrast to the second scenario where the metal reached the cytoplasm in four out of five simulations. This result may suggest a role for the M2 metal (Zn^{2+} or a different type of metal[52]) in facilitating metal movement out of the M1 site, which is conceivable given the likely strong

electrostatic repulsion between two divalent cations due to the short distance between them (4.4 Å in 5TSB). The metal was released into the periplasm in two simulations where the elevator motion of the transport domain was observed again in a manner similar to what has been observed in the second and third scenarios (**Figures S10B** & **S10C**). Close inspection of the resulting OFC-like structures showed that the cytoplasmic gate of the tunnel was not fully closed. To examine whether the folded IL2 disrupts the closing of the tunnel, we unfolded the IL2 and deleted the metal at the M3 site from the OFC-like model. After running a standard MD simulation for 1 μs, it was found that the movement of the portions of TM4 and TM5 on the cytoplasmic side led to the closing of the cytoplasmic gate composed of a few hydrophobic residues (**Figure S11**).

Overall, the MTD simulations: (1) established the details of metal release from the transport site into the cytoplasm and the roles of conserved residues (including E276) along the metal release pathway in this process; (2) supported the proposed function of the IL2 as an activity regulator; (3) provided evidence supporting the role of the M2 metal in facilitating metal release from the M1 site; and importantly, (4) revealed an IFC-to-OFC transition through a combination of a vertical sliding and the hinge motion of the transport domain. Computationally revealing such a global conformational change is unprecedented for elevator transporters.

Metal substrate binding facilitated IFC-to-OFC conformational switch

The MTD simulations showed a clear correlation between the direction of the metal movement and the elevator motion of the transport domain (**Table S2**), but it is unclear whether the metal is the driving force for the elevator motion or whether it takes a free ride on a spontaneous conformational switch[53]. Previously, we have conducted a cysteine accessibility assay to detect the conformational states of BbZIP in the membrane fractions of *E.coli* cells[38]. In this work, we used this approach to investigate the role of metal substrates in determining the conformational states of the transporter. We chose two variants, L200C and A203C, because the single cysteine residue in each variant is accessible to the solvent only when the transporter is in the OFC (**Figure 5A**). As shown in **Figure 5B**, both BbZIP variants preferentially adopted the IFC in the presence of the metal substrates (Zn^{2+} and Cd^{2+}), which was evidenced by less N-ethylmaleimide (NEM) labeling under the native conditions but more mPEG maleimide 5k (mPEG5k) labeling upon denaturation, when compared to the results obtained in the absence of metal. This result indicates that binding of metal substrates significantly increases the population of the IFC. In order to determine which metal binding site(s) are responsible for the metal induced conformational change, we disrupted the M1, M2, or M3 metal binding site in the L200C and A203C variants by replacing the metal chelating residues with alanine residues (**Figure 2**). The resulting six variants, including ΔM1-L200C (H177A/E211A/L200C), ΔM1-A203C (H177A/E211A/A203C), ΔM2-L200C (N178A/D208A/E240A/L200C), ΔM2-A203C (N178A/D208A/E240A/A203C), ΔM3-L200C (H149A/H151A/L200C), and ΔM3-A203C (H149A/H151A/A203C), were applied to the cysteine accessibility assay (**Figure 5B**). In sharp contrast to the variants with a deleted M2 site, disruption of the M1 or M3 site nearly eliminated the effects of metal binding on the accessibility of the introduced cysteine residues, indicating that the metal binding to M1 and M3 sites triggers the formation and maintenance of the IFC whereas metal binding to the M2 site does not. This result supports the notion that the M1 site, but not the M2 site, is the authentic transport site[35] and that metal binding triggers the OFC-to-IFC transition of BbZIP through the charge-compensation mechanism[36,38], highlighting the importance of neutralization of transport site charges by the countercharged substrates in

facilitating the elevator motion of the transport domain against the uncharged scaffold domain[54-57]. It is, however, unexpected that the M3 site, which is not a part of the transport site, is also crucially involved in the substrate induced conformational change. To further the understanding of the role of the M3 site, we incubated the H149A/H151A variant (where the M3 site has been disrupted) in the Cd-bound state with excess Zn^{2+} and determined the Cd/protein molar ratio after the treatment using ICP-MS. The result showed that the H149A/H151A variant barely retained any Cd^{2+} (0.1±0.03 Cd per protein, mean±s.e.m., n=2), whereas wild-type BbZIP with the same treatment still retained 1.3±0.4 Cd per protein molecule (mean±s.e.m., n=2) (**Figure 5C**), indicating that the variant is unable to retain Cd^{2+} bound to the transport site in the presence of a competing substrate (Zn^{2+}). This is likely due to the increased metal release from the transport site, and thus the reduced metal binding to the transporter, upon disruption of the M3 site, which is consistent with the results of the functional study (**Figures 2F**-**H**) and the MTD simulations (**Figure 3**), and the proposed metal release pathways (**Figure 2K**).

Discussion

ZIPs are crucially involved in the homeostasis of a panel of essential trace elements and it is imperative to elucidate their working mechanisms because of the great potential applications in biomedicine, agriculture, and environmental protection. Although BbZIP, a prototype of the ZIP family, has been extensively studied in recent years, key questions regarding the transport mechanism, including the details of the proposed conformational changes and the translocation of the metal substrate through the transporter, remain to be answered. In this work, we addressed these issues by integrating the experimental and computational approaches to gain a thorough understanding of the transport mechanism, which not only reveals an unprecedented elevator transport mode, but also a highly regulated process of metal release from the transport site, providing a paradigm for studying other metal transporters.

Regulated metal release from the transport site into the cytoplasm

Three metal binding sites have been identified in BbZIP (**Figure 2**), including the M1 and M2 sites at the transport site and the M3 site at the end of the metal release tunnel. For BbZIP to function as a metal transporter rather than a metal binding protein, it is critical to efficiently release the metal substrate from these high-affinity binding sites into the cytoplasm. Our experimental and computational studies revealed a metal release mechanism (**Figure 2K**), which is likely conserved in the ZIP family, and also indicated that the metal release process is differentially regulated (**Figure 6**).

At normal (or low) intracellular zinc levels, the metal at the M1 site can move to the unoccupied M3 site via Path 1 (**Figure 2K**). Given that two carboxylic acid residues and one (or two) histidine residue are involved in metal chelation at the M3 site, it is conceivable that Zn^{2+} will be held for a while before it is finally released into the cytoplasm. Indeed, the M3 site is one of the local minima along Path 1 (**Figures 3A** & **S8A**). Consistently, when the corresponding M3-forming residues in hZIP4 (except for D604, which is the equivalent to E276 in BbZIP and essential for the transport activity due to its multiple roles during metal release, **Figures 2H**, **2I, 2K** & **3A**) were substituted with alanine residues, the zinc transport activities were increased (**Figures 2F** & **2G**). In this sense, the M3 site functions as a metal sink that negatively regulates the transport activity by transiently holding the metal substrate. For metal transporters, it is not rare that a cytoplasmic metal binding motif negatively regulates the transport activity. AtMTP1, a

vacuolar Zn^{2+}/H^{+} antiporter from *Arabidopsis thaliana* belonging to the cation diffusion facilitator superfamily, exhibited a greatly increased activity when the cytoplasmic his-rich loop was deleted[58]. Similarly, substitution of the very C-terminal cytoplasmic "His-Cys-His" metal binding motif of the copper transporter CTR1 with alanine residues significantly increased both K_M and turnover rate[59], reminiscent of the 5HA variant of hZIP4 (**Figure 2G**). When the intracellular zinc is elevated to the level that the M3 site is saturated, the MTD simulations showed that Zn^{2+} at the M1 site can be released into the cytoplasm only through Path 2 (**Figures 2K** & **3C**), which is however kinetically unfavorable when compared to Path 1. Therefore, the M3 site may act as an intracellular zinc sensor that auto-inhibits the activity of the transporter upon intracellular zinc overload[37].

Collectively, our data indicate that the transport activity can be differentially regulated by the M3 site through two mechanisms. It functions as a metal sink under normal conditions or a metal sensor for auto-inhibition upon zinc overload, acting overall as a negative regulator of the transport activity. This notion is further supported by the results of the cysteine accessibility assays (**Figure 5**), which demonstrated that metal binding to the M3 site promotes the stability of the IFC, presumably by reducing the rate of metal release from the transport site. Since the structural elements enabling this dual function, including the conserved metal chelating residues (D144 and E276 in BbZIP) and the his-rich cluster in the IL2, are present in most ZIPs, it is likely that the unraveled mechanisms for metal release and regulation are shared among ZIPs. Physiologically, a highly regulated transport, when combined with a slow transport rate[60], may help to control zinc flux more precisely as zinc is known to be a signaling molecule[61].

An unusual elevator transport mode

A hallmark of the elevator transport mode is the rigid-body sliding of the transport domain relative to the scaffold domain, which alternately exposes the transport site carried by the transport domain to the different sides of the membrane. For BbZIP, both the experimentally solved structures and the computational simulations showed that the transport domain can also undergo a hinge motion (**Figures 1E, 4** & **S10)**. As revealed in the MTD simulations, the combined vertical sliding and the unique hinge motion opens the otherwise blocked pathway in the IFC and exposes the transport site to the periplasm (**Figures 4** & **S10**). This conformational change, as illustrated in **Figure 7** and **Video S1**, distinguishes BbZIP from other elevator transporters. A recent study found that the well-characterized elevator transporters share similar structural features (in particular in the transport domain), indicating that they are all homologous, whereas the dissimilarity of BbZIP in structure with these elevator transporters suggests that BbZIP likely utilizes a transport mode distinct from the canonical elevator mode[40]. Indeed, the substantial hinge motion seen in BbZIP is unprecedented in the previously studied elevator transporters[50,51], indicative of an unusual elevator mode. Given the long history of the ZIP family in evolution, the mechanism utilized by BbZIP, and potentially by other ZIPs, may represent an unprecedented ancient variant of the elevator transport mode.

In conclusion, our integrated structural, biochemical, and computational studies elucidated the mechanism for regulated substrate translocation through the transporter and revealed an unusual elevator-type conformational change, improving the understanding of the transport mechanism of the ZIP metal transporter family. In particular, our enhanced sampling simulations revealed how the transporter undergoes a metal-driven IFC-to-OFC switch. To the best of our knowledge, computationally discovering such a conformational change in simulations is unprecedented for elevator transporters. The application of a biasing potential on the substrate

(Zn^{2+}) in the MTD simulations with optimized collective variables is key to achieving the global conformational switch, and we envision that this approach can be widely applied to other transporters, especially those whose major conformational changes are facilitated by substrate binding, as demonstrated in this study (**Figure 5**).

Materials and Methods

Genes, plasmids, mutagenesis, and reagents

The DNA encoding BbZIP (National Center for Biotechnology Information reference code: WP_010926504) was synthesized with optimized codons for *Escherichia coli* (Integrated DNA Technologies) and inserted into the pLW01 vector with a thrombin cleavage site inserted between the N-terminal His-tag and BbZIP. The DNA encoding human ZIP4 (GenBank access number: BC062625) from Mammalian Gene Collection were purchased from GE Healthcare, and inserted into a modified pEGFP-N1 vector (Clontech) in which the downstream EGFP gene was deleted and an HA tag was added at the C-terminus. Site-directed mutagenesis was conducted using the QuikChange® site-directed mutagenesis kit (Agilent) and verified by DNA sequencing. 1-Oleoyl-rac-glycerol (monoolein), N-ethylmaleimide (NEM), 1,10-phenanthroline, Tris (2-carboxyethyl) phosphine (TCEP) were purchased from Sigma-Aldrich. mPEG-Maleimide MW 5k (#PLS-234) was purchased from Creative PEGworks.

Protein expression, purification, and chemical cross-linking

Expression of the A95C/A214C variant of BbZIP was the same as reported[34,38]. In brief, the expression was conducted in the *E.coli* strain C41 (DE3) pLysS (Lucigen) in LBE-5052 autoinduction medium for 24 hours at room temperature. After harvest, spheroplasts were prepared and lysed in the buffer containing 20 mM Hepes (pH 7.3), 300 mM NaCl, 0.25 mM $CdCl_2$, and the cOmplete protease inhibitors (Sigma-Aldrich). n-Dodecyl-β-D-maltoside (DDM, Anatrace) powder was added to solubilize the membrane fraction (final concentration 1.5%, w/v). The His-tagged protein was purified using HisPur Cobalt Resin (Thermo Fisher Scientific) in 20 mM Hepes (pH 7.3), 300 mM NaCl, 5% glycerol, 0.25 mM $CdCl_2$, and 0.1% DDM. The sample was then concentrated and loaded onto a Superdex Increase 200 column (GE Healthcare) equilibrated with the gel filtration buffer containing 10 mM Hepes, pH 7.3, 300 mM NaCl, 5% glycerol, 0.25 mM $CdCl_2$, and 0.05% DDM. 1 mM TCEP was included throughout the purification process except for the size exclusion chromatography. To reduce Cd^{2+} level, the pooled peak fractions were briefly treated with 5 mM EDTA and immediately applied to a PD-10 desalting column (Cytiva) which has been equilibrated with the gel filtration buffer without Cd^{2+}. Careful control of the metal content to avoid metal oversaturation or metal loss from high-affinity binding sites was found to be critical to maintaining the metal-bound IL2 in its folded state. The protein was then mixed with $HgCl_2$ at a 1:10 molar ratio and allowed to incubate at room temperature for 30 minutes before setting up crystallization trays. To confirm a complete Hg^{2+} cross-linking, the sample was analyzed by ICP-MS after desalting to remove free Hg^{2+}. The molar ratio of Hg:protein was found to be 0.95.

To conduct chemical crosslinking in the membrane fraction of the *E.coli* cells expressing wild-type BbZIP or its variants (A95C/A214C, A95C, and A214C), the spheroplast-derived membrane fraction of the cells from 1 liter culture was suspended in 6 ml solution containing 20 mM Hepes, pH 7.3, 300 mM NaCl, and 5% glycerol. 30 uL of the membrane fraction suspension

was treated with the indicated concentrations of $[Cu(II)(1,10\text{-phenanthroline})]_3$ at room temperature for 1 hour. The membrane fraction was washed once to remove excess copper complex before it was dissolved in SDS-PAGE sample loading buffer and applied to a non-reducing SDS-PAGE. The samples were analyzed by Western blot using the custom mouse anti-BbZIP antibody reported previously[38] and an HRP-conjugated anti-mouse immunoglobulin G antibody (Cell Signaling Technology, Catalog# 7076 S) at 1:5000 dilution. The images of the blots visualized by chemiluminescence (VWR) were taken using a Bio-Rad ChemiDoc Imaging System.

Crystallization, data collection, and structure determination

Purified A95C/A214C variant was concentrated to 15 mg/ml and then mixed with the molten monoolein with two coupled syringes at a ratio of 2:3 (protein/monoolein, v/v). All crystallization trials were set up using a Gryphon crystallization robot (Art Robbins Instruments). 50 nl of BbZIP-monoolein mixture covered with 800 nl of well solution was sandwiched with lipidic cubic phase sandwich set (Hampton Research). Stick-shaped crystals appeared after one week under the condition containing 30% PEG200, 100 mM Hepes, pH 7.0, 100 mM NaCl, 100 mM $CaCl_2$, at 21°C and grew to full size in two weeks. Crystals were harvested with a MiTeGen micromesh and flash-frozen in liquid nitrogen. The X-ray diffraction data were collected at the General Medicine and Cancer Institutes Collaborative Access Team (GM/CA-CAT) (23-ID-B/D) at Advanced Photon Source (APS). The diffraction datasets were indexed, integrated, and scaled in HKL2000[62]. The apo state structure was solved in molecular replacement using the previously solved structure (PDB: 5TSB) as the search model in Phenix[63]. Iterative model building and refinement were conducted in COOT[64] and Phenix, respectively. All figures of protein structures were generated by PyMOL v1.3 (Schrödinger LLC).

Mammalian cell culture, transfection, Cell-based zinc transport assay, and Western blot

Human embryonic kidney cells (HEK293T, ATCC, Catalog# CRL-3216) were cultured in Dulbecco's modified eagle medium (DMEM, Thermo Fisher Scientific) supplemented with 10% (v/v) fetal bovine serum (FBS, Thermo Fisher Scientific) and Antibiotic-Antimycotic solution (Thermo Fisher Scientific) at 5% CO_2 and 37°C. Cells were seeded on the polystyrene 24-well trays (Alkali Scientific) for 16 h in the basal medium and transfected with 0.8 µg DNA/well using lipofectamine 2000 (Thermo Fisher Scientific) in DMEM with 10% FBS.

The zinc transport activities of ZIP4 and the variants were tested using the cell-based transport assay. Twenty hours post transfection, cells were washed with the washing buffer (10 mM HEPES, 142 mM NaCl, 5 mM KCl, 10 mM glucose, pH 7.3) followed by incubation with Chelex-treated DMEM media (10% FBS). 5 µM Zn^{2+} (0.05 µCi/well) was added to cells. After incubation at 37°C for 30 min, the plates were transferred on ice and the ice-cold washing buffer with 1 mM EDTA was added to stop metal uptake. The cells were washed twice and pelleted through centrifugation at 120 x g for 5 min before lysis with 0.5% Triton X-100. A Packard Cobra Auto-Gamma counter was used to measure radioactivity. The transport activity was determined by subtracting the radioactivities of ^{65}Zn associated with the cells transfected with the empty vector from those associated with the cells transfected with metal transporters.

hZIP4-HA and the variants expressed on the plasma membrane were determined by cell surface bound anti-HA antibody as reported[65]. In brief, cells were washed twice with Dulbecco's phosphate-buffered saline (DPBS) on ice and then fixed with 4% Formaldehyde for 5 min. Cells were then washed three times in DPBS and incubated with 5 µg/ml anti-HA antibody (Invitrogen,

Catalog# 26183) at 4°C overnight. Cells were washed five times in DPBS to remove unbound antibodies, lysed in SDS-PAGE sample loading buffer, and eventually applied to SDS-PAGE and Western blot.

For Western blot, the samples mixed with the SDS sample loading buffer were heated at 96°C for 10 min before loading on SDS-PAGE gel. The protein bands were transferred to PVDF membranes (Millipore). After being blocked with 5% nonfat dry milk, the membranes were incubated with a mouse anti-HA antibody at 1:5000 dilution (Invitrogen, Catalog# 26183) at 4°C overnight. As loading control, β-actin levels were detected using a rabbit anti-β-actin antibody at 1:5000 dilution (Cell Signaling Technology, Catalog# 4970S). Primary antibodies were detected with an HRP-conjugated anti-mouse immunoglobulin-G at 1:5000 dilution (Cell Signaling Technology, Catalog# 7076S) for ZIP4 or an HRP-conjugated anti-rabbit immunoglobulin-G for β-actin at 1:5000 dilution (Cell Signaling Technology, Catalog# 7074S) by chemiluminescence (VWR). The images of the blots were taken using a Bio-Rad ChemiDoc Imaging System.

Metal content measurement by ICP-MS

Wild-type BbZIP and the H149A/H151A variant were purified as described above and the N-terminal His_6-tag was removed by incubation with thrombin overnight at 4°C before it was loaded to a Superdex Increase 200 column (GE Healthcare) equilibrated with a Cd-free solution containing 10 mM Hepes (pH 7.3), 300 mM NaCl, 5% glycerol, and 0.05% DDM. The peak fractions were pooled and the protein concentrations were measured using Bio-Rad protein assay. To study metal exchange with excess zinc, the Cd-bound wild-type BbZIP and the H149A/H151A variant prepared in the Cd-free solution were treated with 0.25 mM $ZnCl_2$ at room temperature for 30 min and then applied to a Superdex Increase 200 column (GE Healthcare) equilibrated with 10 mM Hepes (pH 7.3), 300 mM NaCl, 5% glycerol, 0.05% DDM, and 0.25 mM $ZnCl_2$. The peak fractions were pooled and the protein concentrations were measured using Bio-Rad protein assay. To prepare samples for ICP-MS analysis, 50 µl protein sample was mixed with 100 µl of 70% nitric acid (Fisher chemical, Cat# A509P212) in 15 ml metal-free tube (Labcon, Cat# 3134-345-001-9). The samples were heated in a 60°C water bath for 1 h before being diluted to 3 ml using MilliQ water. Samples were analyzed using the Agilent 8900 Triple Quadrupole ICP-MS equipped with the Agilent SPS 4 Autosampler.

Cysteine accessibility assay

The spheroplast-derived membrane fractions of the *E.coli* cells expressing the BbZIP variants with or without the treatment of 50 µM metal ($ZnCl_2$ or $CdCl_2$) were incubated with the indicated concentrations of NEM at 4°C for 1 h, washed twice with a solution containing 100 mM Tris (pH 7.0), 60 mM NaCl, and 10 mM KCl (to remove excess NEM), and then dissolved in the denaturing solution containing 6 M urea, 0.5% SDS, and 0.5 mM DTT (to quench any residual NEM) by gentle shaking at room temperature for 15 minutes. The samples were then treated with mPEG5K at a final concentration of 5 mM to label the unmodified cysteine residue at room temperature for 1 h before they were mixed with 4xSDS-PAGE sample loading buffer containing 20% β-mercaptoethanol (β-ME) and subjected to SDS-PAGE. The custom mouse anti-BbZIP monoclonal antibody was used to detect BbZIP in Western blots and HRP-conjugated anti-mouse immunoglobulin G antibody was used as the secondary antibody at 1:5000 dilution (Cell Signaling Technology, catalog number 7076S). Images of the blots visualized by chemiluminescence (VWR) were taken using a Bio-Rad ChemiDoc imaging system.

Computational simulations

Standard MD simulations

The cryo-EM structure of BbZIP dimer was used as the initial model[37], and the cadmium ions were substituted with zinc ions. The equilibrated system was then compared to the Cd-bound structure, showing that the protein structure did not undergo significant conformational changes upon metal replacement (**Figure S7B**). Next, the optimized C_4 terms were incorporated into the system to enhance the interactions between the metal ions-ligands (carboxylic acid residues and histidine) and the metal ion-water complexes using the parameters developed by Merz group[47,48]. The recently developed C_4 terms for divalent metal ion-ligands can accurately reproduce the experimental free energy interactions between metal ions and the negatively charged residues (aspartate and glutamate), as well as the histidine residue[47,48]. The systems were generated using the CHARMM-GUI server[66], employing the TIP3P water model, with potassium and chloride used as counterions for system neutralization. To mimic the lipid bilayers of gram-negative bacteria, 200 lipid molecules, composed of a 3:1 ratio of POPE to POPG, were employed. Following this, a five-stage minimization process was carried out to optimize the simulation system. Afterwards, a 5 ns NVT ensemble simulation followed by a 5 ns NPT ensemble simulation was conducted to equilibrate the system. The equilibrated system was then subjected to for 2 μs standard MD simulations, and the entire trajectory was analyzed. The SHAKE[67] and Langevin dynamics algorithms were applied to constrain all covalent and hydrogen bonds and maintain the temperature at 303 K, respectively. Pressure control was achieved using isotropic pressure scaling and the Berendsen barostat[68]. All MD simulations were performed using the AMBER 22 package[69], applying both the ff19SB[70] and Lipid21[71] force fields. A time step of 0.002 ps and a nonbonded cutoff of 9 Å were applied in the simulations.

Steered molecular dynamics (SMD)

The Zn-bound model derived from the cryo-EM structure of BbZIP dimer was generated as described above. Four rounds of minimization were carried out to reduce the system's energy, with 10,000 steps of the steepest descent used in each round. The system was then gradually heated to 303 K over 1 ns using a NVT ensemble. Following this, an NPT ensemble was employed for a 4 ns simulation. Then, 100 ns SMD simulations were conducted to pull the folded loop towards the cytosol, applying a force constant of 1000 kcal/(mol*Å^2). Bond lengths, including those involving hydrogen atoms, were constrained using the SHAKE algorithm[67]. Temperature regulation was achieved using the Langevin dynamics thermostat. A nonbonded cutoff distance of 10 Å was applied and Monte Carlo barostat[72] was employed to maintain the desired pressure by regulating the system volume. The simulations were performed with a time step of 0.002 ps and a nonbonded cutoff of 9 Å.

Metadynamics Simulations

Well-tempered (WT) volumetric-based metadynamics (MTD) simulation approach, using spherical coordinates of the metal ion (ρ, θ, and φ) with respect to the center of mass of the group of atoms comprising TM2, TM4, TM5, and TM7 as collective variables (CVs), was employed, following the methodology outlined in prior studies[46,73]. The WT-MTD method has been effectively used to uncover the detailed mechanism of action of the sodium-potassium-chloride cotransporter 1 (NKCC1)[46]. ρ represents the distance of the metal ion from the center of mass of the TMs mentioned above. θ is defined as the polar angle, and φ as the azimuthal angle. The movement of the metal ion away from its binding site was biased using parameters consistent with previous research (deposition time = 5 ps, hill height = 1.0 kJ/mol, σ_{rho} = 0.5 Å,

σ_{theta} = π/16, σ_{phi} = π/8, and bias factor = 10)[46]. Each WT-MTD simulation was repeated at least three times, with a duration of at least 500 ns. The sampling space of CV ρ was confined by restraining to 25 Å, corresponding to a distance where the metal ion can be found fully solvated outside the transporter.

In order to explain and better represent the metal ion movement along the transporter, an additional CV monitoring the coordination number (CN) of the zinc ion (group A) with the transporter heavy atoms (group B) has been employed. The formula used to define this CV is:

$$CN = \sum_{i \in A} \sum_{j \in B} \frac{1 - \left(\frac{r_{ij}}{r_0}\right)^n}{1 - \left(\frac{r_{ij}}{r_0}\right)^m}$$

Where a cutoff of r_0=4 Å has been used to define a contact, together with the powers being set to n=8 and m=16.

Free energy profiles were extracted after reweighting, which relied on two variables: the distance of the zinc ions from the reference center, labeled as CV1 (ρ), and the CN, defined above, as CV2.

All MTD simulation systems were equilibrated using the same method described in the Standard MD Simulations section. The density and temperature of each system were calculated during the last 1 ns of the equilibration phase to confirm that the system had equilibrated properly (**Figures S12** & **S13**). The equilibrated systems were then used to perform the MTD production runs, with the lengths detailed in Table S2. The MTD analyses were performed on the entire trajectories. The PLUMED v.2.8 plugin[74,75] was used to conduct the MTD simulations. Detailed information about the simulation systems for each scenario and their convergence is presented in **Table S3** and **Figure S14**, respectively.

Using other biased sampling techniques, such as umbrella sampling, did not yield the desired results for the system under investigation in this study. Our umbrella sampling results indicated that the helices in contact with the metal ion either significantly or partially unfolded as the metal ion traversed the transporter, revealing very high energy barriers for the metal movement through the transporter.

Standard MD simulations after MTD simulations

To test whether the folded IL2 disrupts the closing of the cytoplasmic gate in the OFC-like conformation, the last snapshots of the relevant MTD simulations, in which Zn^{2+} has been released into the periplasm, were taken and used to perform standard MD simulations for 1 μs after unfolding of the IL2 in SMD as described above and energy minimization/equilibration.

Acknowledgments

We thank the beamline scientists at GM/CA-CAT at APS for the assistance in data collections. We thank the following funding that supported this work: NIH GM129004 and GM140931 (to J.H.), and GM130641 (to K.M.).

Author Contributions

J.H. and K.M. conceived and designed the project. Y.Z., T.Z., and D.S. conducted structural and biochemical experiments. M.J. and L.C. conducted computational simulations. Y.Z., M.J., T.Z., L.S., K.M., and J.H. analyzed the data and wrote the manuscript.

Conflicting Interests

The authors declare that they have no competing interests.

Data and Material Availability

The atomic coordinates and structure factors have been deposited in the Protein Data Bank with the access code of 8J1M. The atomic coordinates of other involved structures can be retrieved from PDB with the access codes of 5TSB, 5TSA, 7Z6M, 7Z6N, and 8GHT. All the results of the computational simulations are available at https://zenodo.org/records/11103168. Source Data are provided with this paper. The data to generate Figures 1B & 1C, Figures 2C & 2F-2J and Figures 5B & 5C are available in Source Data 1.xlsx and Source Data 2.pptx. No restrictions on the availability of any data.

Code Availability

The custom codes required to reproduce all the simulation analyses in the current work are accessible via https://gitlab.msu.edu/jafarima/zip-transporter.git.

Supplemental Information

Document S1 – Figures S1-S14 and Tables S1-S3
Video S1. Elevator-type transport mechanism of BbZIP, related to Figure 7

References

1. Hara, T., Takeda, T.A., Takagishi, T., Fukue, K., Kambe, T., and Fukada, T. (2017). Physiological roles of zinc transporters: molecular and genetic importance in zinc homeostasis. J Physiol Sci *67*, 283-301. 10.1007/s12576-017-0521-4.
2. Kambe, T., Taylor, K.M., and Fu, D. (2021). Zinc transporters and their functional integration in mammalian cells. J Biol Chem *296*, 100320. 10.1016/j.jbc.2021.100320.
3. Hu, J. (2021). Toward unzipping the ZIP metal transporters: structure, evolution, and implications on drug discovery against cancer. FEBS J *288*, 5805-5825. 10.1111/febs.15658.
4. Kury, S., Dreno, B., Bezieau, S., Giraudet, S., Kharfi, M., Kamoun, R., and Moisan, J.P. (2002). Identification of SLC39A4, a gene involved in acrodermatitis enteropathica. Nat Genet *31*, 239-240. 10.1038/ng913.
5. Kury, S., Kharfi, M., Kamoun, R., Taieb, A., Mallet, E., Baudon, J.J., Glastre, C., Michel, B., Sebag, F., Brooks, D., et al. (2003). Mutation spectrum of human SLC39A4 in a panel of patients with acrodermatitis enteropathica. Hum Mutat *22*, 337-338. 10.1002/humu.9178.
6. Fukada, T., Civic, N., Furuichi, T., Shimoda, S., Mishima, K., Higashiyama, H., Idaira, Y., Asada, Y., Kitamura, H., Yamasaki, S., et al. (2008). The zinc transporter SLC39A13/ZIP13 is required for connective tissue development; its involvement in BMP/TGF-beta signaling pathways. PLoS One *3*, e3642. 10.1371/journal.pone.0003642.
7. Bin, B.H., Hojyo, S., Hosaka, T., Bhin, J., Kano, H., Miyai, T., Ikeda, M., Kimura-Someya, T., Shirouzu, M., Cho, E.G., et al. (2014). Molecular pathogenesis of spondylocheirodysplastic Ehlers-Danlos syndrome caused by mutant ZIP13 proteins. EMBO Mol Med *6*, 1028-1042. 10.15252/emmm.201303809.
8. Boycott, K.M., Beaulieu, C.L., Kernohan, K.D., Gebril, O.H., Mhanni, A., Chudley, A.E., Redl, D., Qin, W., Hampson, S., Kury, S., et al. (2015). Autosomal-Recessive Intellectual Disability with Cerebellar Atrophy Syndrome Caused by Mutation of the Manganese and Zinc Transporter Gene SLC39A8. Am J Hum Genet *97*, 886-893. 10.1016/j.ajhg.2015.11.002.
9. Park, J.H., Hogrebe, M., Gruneberg, M., DuChesne, I., von der Heiden, A.L., Reunert, J., Schlingmann, K.P., Boycott, K.M., Beaulieu, C.L., Mhanni, A.A., et al. (2015). SLC39A8 Deficiency: A Disorder of Manganese Transport and Glycosylation. Am J Hum Genet *97*, 894-903. 10.1016/j.ajhg.2015.11.003.
10. Li, M., Zhang, Y., Bharadwaj, U., Zhai, Q.J., Ahern, C.H., Fisher, W.E., Brunicardi, F.C., Logsdon, C.D., Chen, C., and Yao, Q. (2009). Down-regulation of ZIP4 by RNA interference inhibits pancreatic cancer growth and increases the survival of nude mice with pancreatic cancer xenografts. Clin Cancer Res *15*, 5993-6001. 10.1158/1078-0432.CCR-09-0557.
11. Weaver, B.P., Zhang, Y., Hiscox, S., Guo, G.L., Apte, U., Taylor, K.M., Sheline, C.T., Wang, L., and Andrews, G.K. (2010). Zip4 (Slc39a4) expression is activated in hepatocellular carcinomas and functions to repress apoptosis, enhance cell cycle and increase migration. PLoS One *5*. 10.1371/journal.pone.0013158.
12. Matsui, C., Takatani-Nakase, T., Hatano, Y., Kawahara, S., Nakase, I., and Takahashi, K. (2017). Zinc and its transporter ZIP6 are key mediators of breast cancer cell survival under high glucose conditions. FEBS Lett *591*, 3348-3359. 10.1002/1873-3468.12797.
13. Franklin, R.B., Feng, P., Milon, B., Desouki, M.M., Singh, K.K., Kajdacsy-Balla, A., Bagasra, O., and Costello, L.C. (2005). hZIP1 zinc uptake transporter down regulation and zinc depletion in prostate cancer. Mol Cancer *4*, 32. 10.1186/1476-4598-4-32.
14. Desouki, M.M., Geradts, J., Milon, B., Franklin, R.B., and Costello, L.C. (2007). hZip2 and hZip3 zinc transporters are down regulated in human prostate adenocarcinomatous glands. Mol Cancer *6*, 37. 10.1186/1476-4598-6-37.

15. Li, M., Zhang, Y., Liu, Z., Bharadwaj, U., Wang, H., Wang, X., Zhang, S., Liuzzi, J.P., Chang, S.M., Cousins, R.J., et al. (2007). Aberrant expression of zinc transporter ZIP4 (SLC39A4) significantly contributes to human pancreatic cancer pathogenesis and progression. Proc Natl Acad Sci U S A *104*, 18636-18641. 10.1073/pnas.0709307104.
16. Zhao, L., Oliver, E., Maratou, K., Atanur, S.S., Dubois, O.D., Cotroneo, E., Chen, C.N., Wang, L., Arce, C., Chabosseau, P.L., et al. (2015). The zinc transporter ZIP12 regulates the pulmonary vascular response to chronic hypoxia. Nature *524*, 356-360. 10.1038/nature14620.
17. Nolin, E., Gans, S., Llamas, L., Bandyopadhyay, S., Brittain, S.M., Bernasconi-Elias, P., Carter, K.P., Loureiro, J.J., Thomas, J.R., Schirle, M., et al. (2019). Discovery of a ZIP7 inhibitor from a Notch pathway screen. Nat Chem Biol *15*, 179-188. 10.1038/s41589-018-0200-7.
18. Anzilotti, C., Swan, D.J., Boisson, B., Deobagkar-Lele, M., Oliveira, C., Chabosseau, P., Engelhardt, K.R., Xu, X., Chen, R., Alvarez, L., et al. (2019). An essential role for the Zn(2+) transporter ZIP7 in B cell development. Nat Immunol *20*, 350-361. 10.1038/s41590-018-0295-8.
19. Hogstrand, C., Kille, P., Ackland, M.L., Hiscox, S., and Taylor, K.M. (2013). A mechanism for epithelial-mesenchymal transition and anoikis resistance in breast cancer triggered by zinc channel ZIP6 and STAT3 (signal transducer and activator of transcription 3). Biochem J *455*, 229-237. 10.1042/BJ20130483.
20. Taylor, K.M., Muraina, I.A., Brethour, D., Schmitt-Ulms, G., Nimmanon, T., Ziliotto, S., Kille, P., and Hogstrand, C. (2016). Zinc transporter ZIP10 forms a heteromer with ZIP6 which regulates embryonic development and cell migration. Biochem J *473*, 2531-2544. 10.1042/BCJ20160388.
21. Nimmanon, T., Ziliotto, S., Ogle, O., Burt, A., Gee, J.M.W., Andrews, G.K., Kille, P., Hogstrand, C., Maret, W., and Taylor, K.M. (2020). The ZIP6/ZIP10 heteromer is essential for the zinc-mediated trigger of mitosis. Cell Mol Life Sci. 10.1007/s00018-020-03616-6.
22. Sussman, D., Smith, L.M., Anderson, M.E., Duniho, S., Hunter, J.H., Kostner, H., Miyamoto, J.B., Nesterova, A., Westendorf, L., Van Epps, H.A., et al. (2014). SGN-LIV1A: a novel antibody-drug conjugate targeting LIV-1 for the treatment of metastatic breast cancer. Mol Cancer Ther *13*, 2991-3000. 10.1158/1535-7163.MCT-13-0896.
23. Nagayama, A., Vidula, N., Ellisen, L., and Bardia, A. (2020). Novel antibody-drug conjugates for triple negative breast cancer. Ther Adv Med Oncol *12*, 1758835920915980. 10.1177/1758835920915980.
24. Zhang, Y., Bharadwaj, U., Logsdon, C.D., Chen, C., Yao, Q., and Li, M. (2010). ZIP4 regulates pancreatic cancer cell growth by activating IL-6/STAT3 pathway through zinc finger transcription factor CREB. Clin Cancer Res *16*, 1423-1430. 10.1158/1078-0432.CCR-09-2405.
25. Zhang, Y., Chen, C., Yao, Q., and Li, M. (2010). ZIP4 upregulates the expression of neuropilin-1, vascular endothelial growth factor, and matrix metalloproteases in pancreatic cancer cell lines and xenografts. Cancer Biol Ther *9*, 236-242.
26. Lin, Y., Chen, Y., Wang, Y., Yang, J., Zhu, V.F., Liu, Y., Cui, X., Chen, L., Yan, W., Jiang, T., et al. (2013). ZIP4 is a novel molecular marker for glioma. Neuro Oncol *15*, 1008-1016. 10.1093/neuonc/not042.
27. Zhang, Y., Yang, J., Cui, X., Chen, Y., Zhu, V.F., Hagan, J.P., Wang, H., Yu, X., Hodges, S.E., Fang, J., et al. (2013). A novel epigenetic CREB-miR-373 axis mediates ZIP4-induced pancreatic cancer growth. EMBO Mol Med *5*, 1322-1334. 10.1002/emmm.201302507.
28. Cui, X., Zhang, Y., Yang, J., Sun, X., Hagan, J.P., Guha, S., and Li, M. (2014). ZIP4 confers resistance to zinc deficiency-induced apoptosis in pancreatic cancer. Cell Cycle *13*, 1180-1186. 10.4161/cc.28111.
29. Xu, C., Wallace, M.B., Yang, J., Jiang, L., Zhai, Q., Zhang, Y., Hong, C., Chen, Y., Frank, T.S., Stauffer, J.A., et al. (2014). ZIP4 is a novel diagnostic and prognostic marker in human pancreatic

cancer: a systemic comparison between EUS-FNA and surgical specimens. Curr Mol Med *14*, 309-315.

30. Zhang, Q., Sun, X., Yang, J., Ding, H., LeBrun, D., Ding, K., Houchen, C.W., Postier, R.G., Ambrose, C.G., Li, Z., et al. (2015). ZIP4 silencing improves bone loss in pancreatic cancer. Oncotarget *6*, 26041-26051. 10.18632/oncotarget.4667.
31. Fan, Q., Cai, Q., Li, P., Wang, W., Wang, J., Gerry, E., Wang, T.L., Shih, I.M., Nephew, K.P., and Xu, Y. (2017). The novel ZIP4 regulation and its role in ovarian cancer. Oncotarget *8*, 90090-90107. 10.18632/oncotarget.21435.
32. Fan, Q., Zhang, W., Emerson, R.E., and Xu, Y. (2020). ZIP4 Is a Novel Cancer Stem Cell Marker in High-Grade Serous Ovarian Cancer. Cancers (Basel) *12*. 10.3390/cancers12123692.
33. Anzilotti, C., Swan, D.J., Boisson, B., Deobagkar-Lele, M., Oliveira, C., Chabosseau, P., Engelhardt, K.R., Xu, X., Chen, R., Alvarez, L., et al. (2019). An essential role for the Zn2+ transporter ZIP7 in B cell development. Nature Immunology. 10.1038/s41590-018-0295-8.
34. Zhang, T., Liu, J., Fellner, M., Zhang, C., Sui, D., and Hu, J. (2017). Crystal structures of a ZIP zinc transporter reveal a binuclear metal center in the transport pathway. Sci Adv *3*, e1700344. 10.1126/sciadv.1700344.
35. Zhang, T., Sui, D., Zhang, C., Cole, L., and Hu, J. (2020). Asymmetric functions of a binuclear metal center within the transport pathway of a human zinc transporter ZIP4. FASEB J *34*, 237-247. 10.1096/fj.201902043R.
36. Wiuf, A., Steffen, J.H., Becares, E.R., Gronberg, C., Mahato, D.R., Rasmussen, S.G.F., Andersson, M., Croll, T., Gotfryd, K., and Gourdon, P. (2022). The two-domain elevator-type mechanism of zinc-transporting ZIP proteins. Sci Adv *8*, eabn4331. 10.1126/sciadv.abn4331.
37. Pang, C., Chai, J., Zhu, P., Shanklin, J., and Liu, Q. (2023). Structural mechanism of intracellular autoregulation of zinc uptake in ZIP transporters. Nat Commun *14*, 3404. 10.1038/s41467-023-39010-6.
38. Zhang, Y., Jiang, Y., Gao, K., Sui, D., Yu, P., Su, M., Wei, G.W., and Hu, J. (2023). Structural insights into the elevator-type transport mechanism of a bacterial ZIP metal transporter. Nat Commun *14*, 385. 10.1038/s41467-023-36048-4.
39. Pasquadibisceglie, A., Leccese, A., and Polticelli, F. (2022). A computational study of the structure and function of human Zrt and Irt-like proteins metal transporters: An elevator-type transport mechanism predicted by AlphaFold2. Front Chem *10*, 1004815. 10.3389/fchem.2022.1004815.
40. Trebesch, N., and Tajkhorshid, E. (2023). Structure Reveals Homology in Elevator Transporters. bioRxiv. 10.1101/2023.06.14.544989.
41. Gao, X., Dong, X., Li, X., Liu, Z., and Liu, H. (2020). Prediction of disulfide bond engineering sites using a machine learning method. Sci Rep *10*, 10330. 10.1038/s41598-020-67230-z.
42. Gyimesi, G., Albano, G., Fuster, D.G., Hediger, M.A., and Pujol-Gimenez, J. (2019). Unraveling the structural elements of pH sensitivity and substrate binding in the human zinc transporter SLC39A2 (ZIP2). J Biol Chem *294*, 8046-8063. 10.1074/jbc.RA118.006113.
43. Grazioso, G., Limongelli, V., Branduardi, D., Novellino, E., De Micheli, C., Cavalli, A., and Parrinello, M. (2012). Investigating the mechanism of substrate uptake and release in the glutamate transporter homologue Glt(Ph) through metadynamics simulations. J Am Chem Soc *134*, 453-463. 10.1021/ja208485w.
44. Janos, P., Aupic, J., Ruthstein, S., and Magistrato, A. (2022). The conformational plasticity of the selectivity filter methionines controls the in-cell Cu(I) uptake through the CTR1 transporter. QRB Discov *3*, e3. 10.1017/qrd.2022.2.
45. Abellon-Ruiz, J., Jana, K., Silale, A., Frey, A.M., Basle, A., Trost, M., Kleinekathofer, U., and van den Berg, B. (2023). BtuB TonB-dependent transporters and BtuG surface lipoproteins form

stable complexes for vitamin B(12) uptake in gut Bacteroides. Nat Commun *14*, 4714. 10.1038/s41467-023-40427-2.

46. Janos, P., and Magistrato, A. (2021). All-Atom Simulations Uncover the Molecular Terms of the NKCC1 Transport Mechanism. J Chem Inf Model *61*, 3649-3658. 10.1021/acs.jcim.1c00551.
47. Li, Z., Song, L.F., Sharma, G., Koca Findik, B., and Merz, K.M., Jr. (2022). Accurate Metal-Imidazole Interactions. J Chem Theory Comput. 10.1021/acs.jctc.2c01081.
48. Jafari, M., Li, Z., Song, L.F., Sagresti, L., Brancato, G., and Merz, K. (2024). Thermodynamics of Metal–Acetate Interactions. J Phys Chem B *128*, 684-697.
49. Sharma, G., and Merz, K.M. (2021). Formation of the Metal-Binding Core of the ZRT/IRT-like Protein (ZIP) Family Zinc Transporter. Biochemistry *60*, 2727-2738. 10.1021/acs.biochem.1c00415.
50. Garaeva, A.A., and Slotboom, D.J. (2020). Elevator-type mechanisms of membrane transport. Biochem Soc Trans *48*, 1227-1241. 10.1042/BST20200290.
51. Drew, D., and Boudker, O. (2016). Shared Molecular Mechanisms of Membrane Transporters. Annu Rev Biochem *85*, 543-572. 10.1146/annurev-biochem-060815-014520.
52. Roberts, C.S., Ni, F., and Mitra, B. (2021). The Zinc and Iron Binuclear Transport Center of ZupT, a ZIP Transporter from Escherichia coli. Biochemistry *60*, 3738-3752. 10.1021/acs.biochem.1c00621.
53. Latorraca, N.R., Fastman, N.M., Venkatakrishnan, A.J., Frommer, W.B., Dror, R.O., and Feng, L. (2017). Mechanism of Substrate Translocation in an Alternating Access Transporter. Cell *169*, 96-107 e112. 10.1016/j.cell.2017.03.010.
54. Law, C.J., Enkavi, G., Wang, D.N., and Tajkhorshid, E. (2009). Structural basis of substrate selectivity in the glycerol-3-phosphate: phosphate antiporter GlpT. Biophys J *97*, 1346-1353. 10.1016/j.bpj.2009.06.026.
55. Grewer, C., Zhang, Z., Mwaura, J., Albers, T., Schwartz, A., and Gameiro, A. (2012). Charge compensation mechanism of a Na+-coupled, secondary active glutamate transporter. J Biol Chem *287*, 26921-26931. 10.1074/jbc.M112.364059.
56. Nath, S. (2021). Charge transfer across biomembranes: A solution to the conundrum of high desolvation free energy penalty in ion transport. Biophys Chem *275*, 106604. 10.1016/j.bpc.2021.106604.
57. Sauer, D.B., Wang, B., Sudar, J.C., Song, J., Marden, J., Rice, W.J., and Wang, D.N. (2022). The ups and downs of elevator-type di-/tricarboxylate membrane transporters. FEBS J *289*, 1515-1523. 10.1111/febs.16158.
58. Kawachi, M., Kobae, Y., Mimura, T., and Maeshima, M. (2008). Deletion of a histidine-rich loop of AtMTP1, a vacuolar Zn(2+)/H(+) antiporter of Arabidopsis thaliana, stimulates the transport activity. J Biol Chem *283*, 8374-8383. 10.1074/jbc.M707646200.
59. Maryon, E.B., Molloy, S.A., Ivy, K., Yu, H., and Kaplan, J.H. (2013). Rate and regulation of copper transport by human copper transporter 1 (hCTR1). J Biol Chem *288*, 18035-18046. 10.1074/jbc.M112.442426.
60. Lin, W., Chai, J., Love, J., and Fu, D. (2010). Selective electrodiffusion of zinc ions in a Zrt-, Irt-like protein, ZIPB. J Biol Chem *285*, 39013-39020. 10.1074/jbc.M110.180620.
61. Hojyo, S., and Fukada, T. (2016). Zinc transporters and signaling in physiology and pathogenesis. Arch Biochem Biophys *611*, 43-50. 10.1016/j.abb.2016.06.020.
62. Otwinowski, Z., and Minor, W. (1997). Processing of X-ray diffraction data collected in oscillation mode. Macromolecular Crystallography, Pt A *276*, 307-326. Doi 10.1016/S0076-6879(97)76066-X.
63. Liebschner, D., Afonine, P.V., Baker, M.L., Bunkoczi, G., Chen, V.B., Croll, T.I., Hintze, B., Hung, L.W., Jain, S., McCoy, A.J., et al. (2019). Macromolecular structure determination using X-rays,

neutrons and electrons: recent developments in Phenix. Acta Crystallogr D Struct Biol *75*, 861-877. 10.1107/S2059798319011471.

64. Emsley, P., Lohkamp, B., Scott, W.G., and Cowtan, K. (2010). Features and development of Coot. Acta Crystallogr D Biol Crystallogr *66*, 486-501. 10.1107/S0907444910007493.
65. Zhang, T., Sui, D., and Hu, J. (2016). Structural insights of ZIP4 extracellular domain critical for optimal zinc transport. Nat Commun *7*, 11979. 10.1038/ncomms11979.
66. Lee, J., Patel, D.S., Stahle, J., Park, S.J., Kern, N.R., Kim, S., Lee, J., Cheng, X., Valvano, M.A., Holst, O., et al. (2019). CHARMM-GUI Membrane Builder for Complex Biological Membrane Simulations with Glycolipids and Lipoglycans. J Chem Theory Comput *15*, 775-786. 10.1021/acs.jctc.8b01066.
67. Ryckaert, J., Ciccotti, G., and Berendsen, H. (1977). Numerical integration of the cartesian equations of motion of a system with constraints: molecular dynamics of n-alkanes. J Comput Phys *23*, 327–341.
68. Berendsen, H.J.C., Postma, J.P.M., van Gunsteren, W.F., DiNola, A., and Haak, J.R. (1984). Molecular dynamics with coupling to an external bath. J Chem Phys *81*, 3684–3690.
69. Case, D.A., Aktulga, H.M., Belfon, K., Cerutti, D.S., Cisneros, G.A., Cruzeiro, V.W.D., Forouzesh, N., Giese, T.J., Gotz, A.W., Gohlke, H., et al. (2023). AmberTools. J Chem Inf Model *63*, 6183-6191. 10.1021/acs.jcim.3c01153.
70. Tian, C., Kasavajhala, K., Belfon, K.A.A., Raguette, L., Huang, H., Migues, A.N., Bickel, J., Wang, Y., Pincay, J., Wu, Q., and Simmerling, C. (2020). ff19SB: Amino-Acid-Specific Protein Backbone Parameters Trained against Quantum Mechanics Energy Surfaces in Solution. J Chem Theory Comput *16*, 528-552. 10.1021/acs.jctc.9b00591.
71. Dickson, C.J., Walker, R.C., and Gould, I.R. (2022). Lipid21: Complex Lipid Membrane Simulations with AMBER. J Chem Theory Comput *18*, 1726-1736. 10.1021/acs.jctc.1c01217.
72. Åqvist, J., Wennerström, P., Nervall, M., Bjelic, S., and Brandsdal, B.O. (2004). Molecular dynamics simulations of water and biomolecules with a Monte Carlo constant pressure algorithm. Chem Phys Lett *384*, 288–294.
73. Capelli, R., Carloni, P., and Parrinello, M. (2019). Exhaustive Search of Ligand Binding Pathways via Volume-Based Metadynamics. J Phys Chem Lett *10*, 3495-3499. 10.1021/acs.jpclett.9b01183.
74. Bonomi, M., Branduardi, D., Bussi, G., Camilloni, C., Provasi, D., Raiteri, P., Donadio, D., Marinelli, F., Pietrucci, F., Broglia, R.A., and Parrinello, M. (2009). PLUMED: A portable plugin for free-energy calculations with molecular dynamics. Computer Physics Communications *180*, 1961-1972. 10.1016/j.cpc.2009.05.011.
75. Tribello, G.A., Bonomi, M., Branduardi, D., Camilloni, C., and Bussi, G. (2014). PLUMED 2: New feathers for an old bird. Computer Physics Communications *185*, 604-613. 10.1016/j.cpc.2013.09.018.

Figure legends

Figure 1. Chemical cross-linking and structure determination of the A95C/A214C variant. (**A**) A95 and A214 in IFC of BbZIP (PDB: 5TSB). The distance between the C_α atoms (10.1 Å) is greater than the distance required for a disulfide bond (3.0-7.5 Å, ref 41). (**B**) Disulfide bond cross-linking of the variants of A95C/A214C, A95C, A214C, and wild-type BbZIP in the membrane fraction of the *E.coli* cells overexpressing the target proteins by [Cu(II)(1,10-phenanthroline)$_3$] at the indicated concentrations. BbZIP and the variants were detected in Western blot by using a custom mouse monoclonal antibody against BbZIP. (**C**) Cross-linking of the purified variants of A95C/A214C, A95C, and A214C by $HgCl_2$ at the protein:Hg molar ratio of 1:10. Pretreatment with N-ethylmaleimide (NEM) and post-treatment with 2-mercaptoethanol (β-ME) prevented and reversed the cross-linking reaction, respectively. (**D**) Overall structure of the Hg^{2+}-cross-linked A95C/A214C variant. The conserved eight TMs are colored in rainbow and TM0 is in grey. Cd^{2+} at the M1, M2, and M3 sites are depicted as light-brown spheres, and Hg^{2+} is shown as a grey sphere. (**E**) Hinge motion of the transport domain. The scaffold domains of BbZIP (green) in representative structures are aligned with selected C_α atoms shown in sphere mode. When compared to the Cd-bound state (PDB: 5TSB, blue), the transport domain of the cross-linked variant (red) undergoes an upward/clockwise hinge motion, whereas those in the apo state structures (grey to black) rotate in the opposite direction. The arrows indicate the opposite directions of the hinge motion from the Cd-bound state.

Figure 2. Metal binding to BbZIP and metal release from the transport site. (**A**) Metal binding at the transport site of the A95C/A214C variant. *Left*: Cd^{2+} binding at the M1 and M2 sites and Hg^{2+} binding between C95 and C214. The blue meshes indicate the electron densities of Cd^{2+} and Hg^{2+} (2Fo-Fc map, σ=4). The occupancies are 0.85 and 0.42 for Cd^{2+} at M1 and M2, and 0.36 for Hg^{2+}, respectively. *Right*: structural comparison of the transport site in the structure of the variant (rainbow color) with that of the Cd^{2+}-bound structure (white, PDB: 5TSB). Note that a chloride ion (green sphere) displaces the sulfur atom of M99 in 5TSB from the coordination sphere at the M1 site. (**B**) The structure of the IL2 and the M3 site. The blue meshes indicate the 2Fo-Fc map (σ=1) of the IL2 and the ordered water molecules (red balls). The occupancy of Cd^{2+} at the M3 site is 0.84. The hydrogen bonds involved in stabilizing the IL2 are shown as yellow dashed lines. The inset shows the zoom-in view of Cd^{2+} binding at the M3 site. The distances between Cd^{2+} and the coordinating atoms are indicated in angstrom. (**C**) Metal content determination of wild-type BbZIP and the H149A/H151A variant. Cd^{2+} was excluded from the running buffer in the final size-exclusion chromatography and the Cd levels in the samples were determined by ICP-MS. The data (Cd per protein, from two independent experiments) are shown as rhomboids, and the horizontal and vertical bars indicate the mean and S.D., respectively. (**D**) Divided metal release tunnel by the folded IL2. From the transport site, the pathway toward the periplasm is blocked by the indicated non-polar residues, whereas the tunnel toward the cytoplasm is divided by the folded IL2 into Path 1 and Path 2, as indicated by the dashed lines. Cd^{2+} are shown as light-brown spheres and the ordered water molecules are depicted as red balls. (**E**) Sequence alignment of BbZIP and human ZIPs. The highlighted residues include D144 and E276 that participate in the M3 site and P279 that contributes to the flexibility of E276. (**F**-**J**) Kinetic study of the hZIP4 variants in the cell-based ^{65}Zn transport assay. Zinc transport activity was calculated by subtracting the radioactivity associated with the cells transfected with the empty vector and calibrated by hZIP4 expression level determined in Western blot experiments. The dose curves were fitted with the Hill model and the kinetic parameters obtained from curve fitting are listed in the tables. The data shown are the results

from one of three independent experiments and three biological replicates (n=3) were tested for each condition in one experiment. The total and cell surface expression of hZIP4 and its variants were detected in Western blot using an anti-HA antibody. (**K**) Metal release pathways. The new structure (blue), the Cd-bound structure (PDB: 7Z6M, green), and the zinc-substituted structure (PDB: 5TSA, pink) are superimposed to reveal the procedure of metal release from the transport site into the cytoplasm. The metal at the M1 site first moves to the transient metal binding site when H177 flips its side chain and E276 joins to coordinate the metal. The downstream path diverges at this point. To enter Path 1, a nearly 90-degree rotation of E276 directs the metal substrate from the transient binding site to the M3 site, which acts as a metal sink, before the metal is released into the cytoplasm. The curved two-headed arrow indicates the flexibility conferred by the helix-breaking residue P279. Alternatively, the metal can move through Path 2.

Figure 3. Metal release from the M1 site into the cytoplasm revealed by MTD simulations. (**A**) Free energy surface map of metal coordination upon metal release via Path 1 in the first scenario. CV1 represents the distance from the metal ion to the protein center of mass, and CV2 is the number of non-hydrogen atoms within 4 Å of the metal. The shown data are from one out of three independent simulations. The results of the other two simulations are shown in Figure S8A. (**B**) Snapshots of the overall structure of the transporter and metal coordination at the selected local minima in (A). The red arrows indicate the vertical positions of the metal when it moved from the M1 site to the M3 site via Path 1. In State V, the metal is bound at the M3 site. (**C**) Structural rearrangements (red arrows) of the IL2 and the cytoplasmic portions of TM4 and TM5 upon metal released into the cytoplasm via Path 2 (dashed curve arrow) in the second scenario. The structural modes before and after metal release into the cytoplasm are colored in orange and green, respectively. The shown data are from one out of four simulations. The results of the other three simulations are shown in Figure S8B.

Figure 4. The IFC-to-OFC transition uncovered in the MTD simulations. (**A**-**C**) Conformational changes of the highlighted structural elements – TM5 (**A**), TM4 (**B**), and TM1/TM6 (**C**). The dark red and yellow-green spheres represent Zn^{2+} before and after the IFC-to-OFC transition, respectively. (**D**) Distance changes between the selected residue pairs throughout the simulation. The Cα atoms of the selected residues are shown as spheres and labeled in the initial IFC model and the OFC-like conformation generated in the simulation. The dashed line indicates the time when the IFC-to-OFC transition occurs at ~180 ns. (**E**) Combination of the vertical sliding (*left*) and the hinge motion (*right*) of the transport domain. The scaffold domains of the representative BbZIP structures are aligned to reveal the conformational changes of the transport domain. The results of the MTD simulations showing the similar IFC-to-OFC transition are shown in Figure S10.

Figure 5. Detection of metal binding induced conformational changes of BbZIP using cysteine accessibility assay. (**A**) Illustration of cysteine labeling with NEM or mPEG5k when BbZIP is in the IFC or OFC. The scaffold domain and transport domain are colored in blue and green, respectively. (**B**) Cysteine accessibility assay of the variants in the presence or absence of metal substrates (50 μM). The membrane fractions of the *E.coli* cells expressing the variants

were treated with the indicated amounts of NEM under native conditions, followed by the treatment of mPEG5k under denaturing conditions. (**C**) Cd content determined by ICP-MS after the treatment of the Cd-bound proteins (wild-type BbZIP and the H149A/H151A variant) in a Cd-free solution (Figure 2C) with excess zinc ions (250 μM). The data (Cd per protein, from two independent experiments) are shown as rhomboids, and the horizontal and vertical bars indicate the mean and S.D., respectively.

Figure 6. Regulated metal release from the transport site into the cytoplasm. (**A**) At normal or low zinc concentration, the metal released from the M1 site preferentially moves through Path 1 via the M3 site, where the histidine residue(s) in the IL2 participates in metal chelation, and is then slowly released into the cytoplasm. The question mark indicates that it is uncertain whether H151 is involved in binding Zn^{2+} during the release process, as it is not suggested by MTD simulation. (**B**) At high intracellular zinc concentration, the M3 site is occupied by a zinc ion from the cytoplasm, which blocks Path 1. Metal can be released into the cytoplasm only through Path 2 at a slower rate. In either scenario, the IL2 negatively regulates the transport activity.

Figure 7. Proposed conformational change during the IFC-to-OFC transition. The scaffold domains (blue) are structurally aligned and the transport domains are shown in orange (IFC) or green (OFC). The transmembrane helices (TM1, TM4, TM5, and TM6) in the transport domain are shown as rectangles. To switch from the IFC to the OFC during a transport cycle, the transport domain undergoes a combined hinge motion (curved arrow) and a vertical sliding (straight arrow), along with the outward swing of the periplasmic portion of TM5 (green 3D arrow) and the inward swing of the cytoplasmic portion of TM4 (light blue 3D arrow).

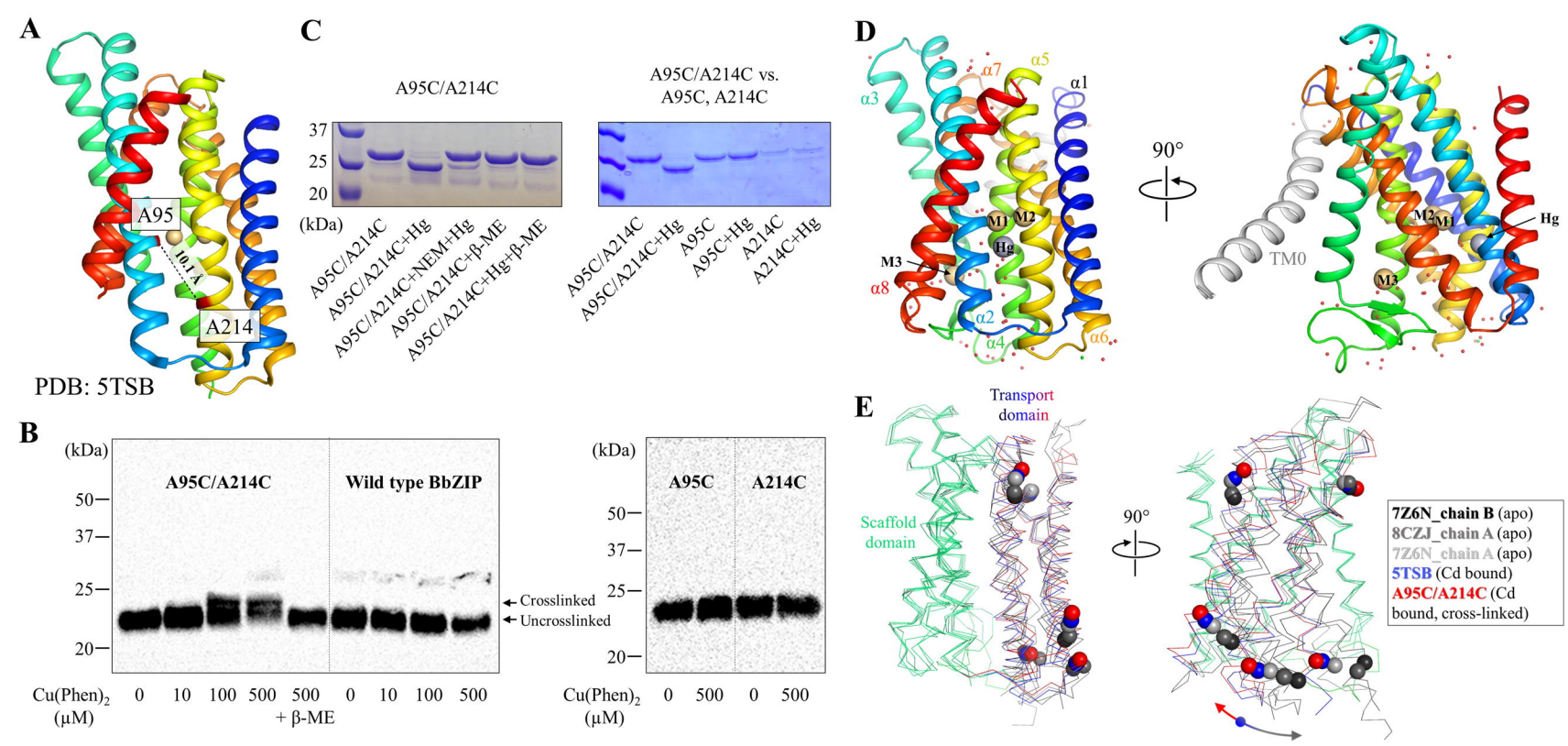
A
A95
10.1 Å
A214
PDB: 5TSB
C
A95C/A214C
37
25
20
(kDa)
A95C/A214C
A95C/A214C+Hg
A95C/A214C+NEM+Hg
A95C/A214C+β-ME
A95C/A214C+Hg+β-ME
A95C/A214C vs.
A95C, A214C
A95C/A214C
A95C/A214C+Hg
A95C
A95C+Hg
A214C
A214C+Hg
B
(kDa)
A95C/A214C
Wild type BbZIP
50
37
25
20
Crosslinked
Uncrosslinked
Cu(Phen)2 (μM)
0 10 100 500 500 0 10 100 500
+ β-ME
(kDa)
A95C
A214C
50
37
25
20
Cu(Phen)2 (μM)
0 500 0 500
D
α3
α7
α5
α1
M1
M2
Hg
M3
α8
α2
α4
α6
90°
TM0
M2
M1
Hg
M3
E
Transport domain
Scaffold domain
90°
7Z6N_chain B (apo)
8CZJ_chain A (apo)
7Z6N_chain A (apo)
5TSB (Cd bound)
A95C/A214C (Cd bound, cross-linked)

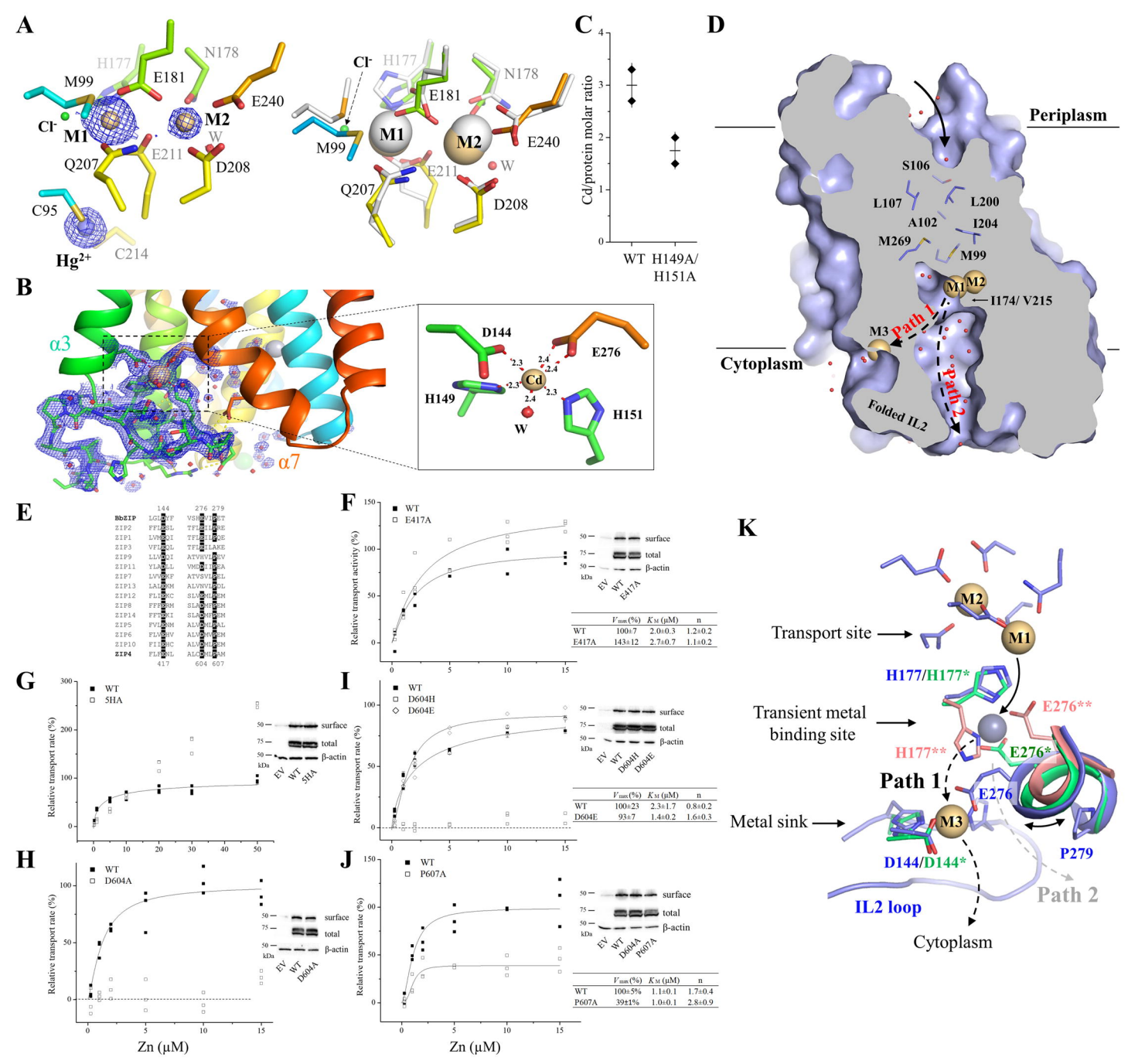
A
H177
N178
M99
E181
E240
Cl-
M1
M2
W
E211
Q207
D208
C95
Hg2+
C214
Cl-
H177
N178
E181
M99
M1
M2
E240
W
E211
Q207
D208
B
α3
α7
D144
E276
2.3
2.4
2.4
Cd
2.3
2.3
H149
2.4
H151
W
C
Cd/protein molar ratio
WT
H149A/
H151A
D
Periplasm
Cytoplasm
S106
L107
L200
A102
I204
M269
M99
M1
M2
I174/ V215
M3
Path 1
Path 2
Folded IL2
E
144
276 279
BbZIP
ZIP2
ZIP1
ZIP3
ZIP9
ZIP11
ZIP7
ZIP13
ZIP12
ZIP8
ZIP14
ZIP5
ZIP6
ZIP10
ZIP4
417
604 607
F
WT
E417A
Relative transport activity (%)
surface
total
β-actin
kDa
EV
WT
E417A
Vmax(%) KM (μM) n
WT 100±7 2.0±0.3 1.2±0.2
E417A 143±12 2.7±0.7 1.1±0.2
G
WT
5HA
Relative transport rate (%)
surface
total
β-actin
kDa
EV
WT
5HA
I
WT
D604H
D604E
Relative transport rate (%)
surface
total
β-actin
kDa
EV
WT
D604H
D604E
Vmax(%) KM (μM) n
WT 100±23 2.3±1.7 0.8±0.2
D604E 93±7 1.4±0.2 1.6±0.3
H
WT
D604A
Relative transport rate (%)
Zn (μM)
surface
total
β-actin
kDa
EV
WT
D604A
J
WT
P607A
Relative transport rate (%)
Zn (μM)
surface
total
β-actin
kDa
EV
WT
D604A
P607A
Vmax(%) KM (μM) n
WT 100±5% 1.1±0.1 1.7±0.4
P607A 39±1% 1.0±0.1 2.8±0.9
K
M2
M1
Transport site
H177/H177*
Transient metal
binding site
E276**
H177**
E276*
Path 1
E276
Metal sink
M3
P279
D144/D144*
Path 2
IL2 loop
Cytoplasm

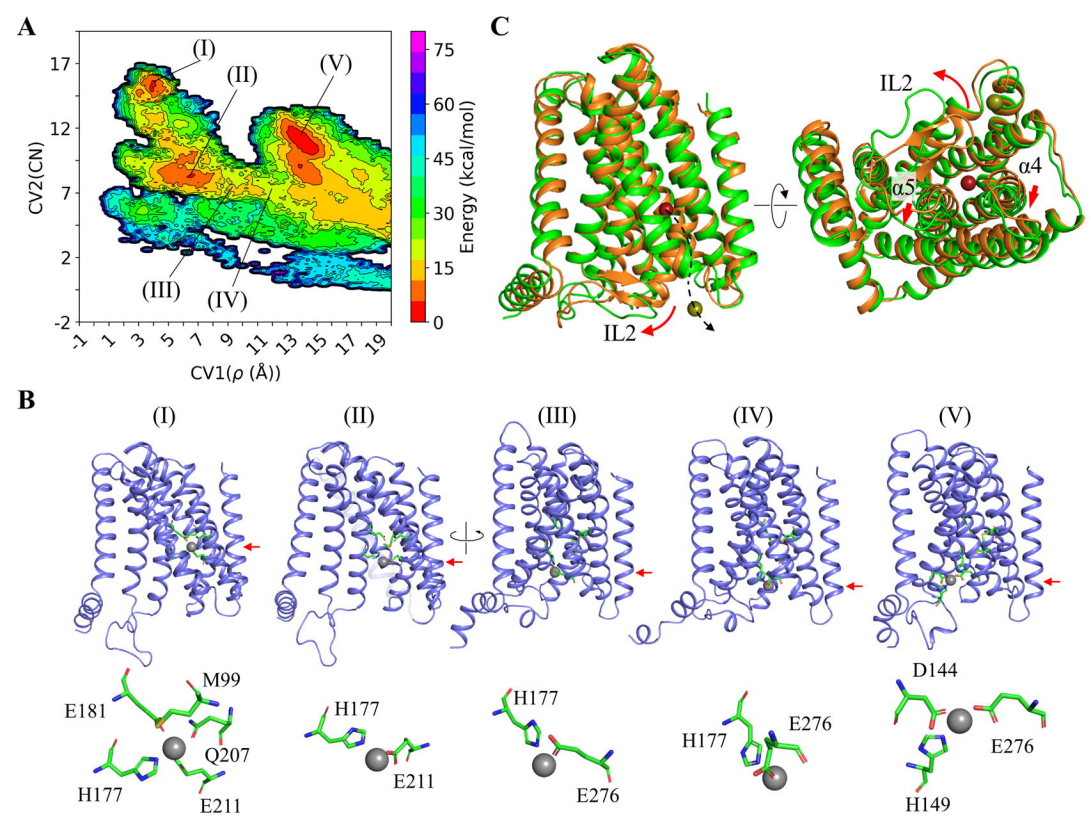
A
(I)
(II)
(V)
(III)
(IV)
CV2(CN)
CV1(ρ (Å))
Energy (kcal/mol)
C
IL2
α4
α5
IL2
B
(I)
(II)
(III)
(IV)
(V)
M99
E181
Q207
H177
E211
H177
E211
H177
E276
H177
E276
D144
E276
H149

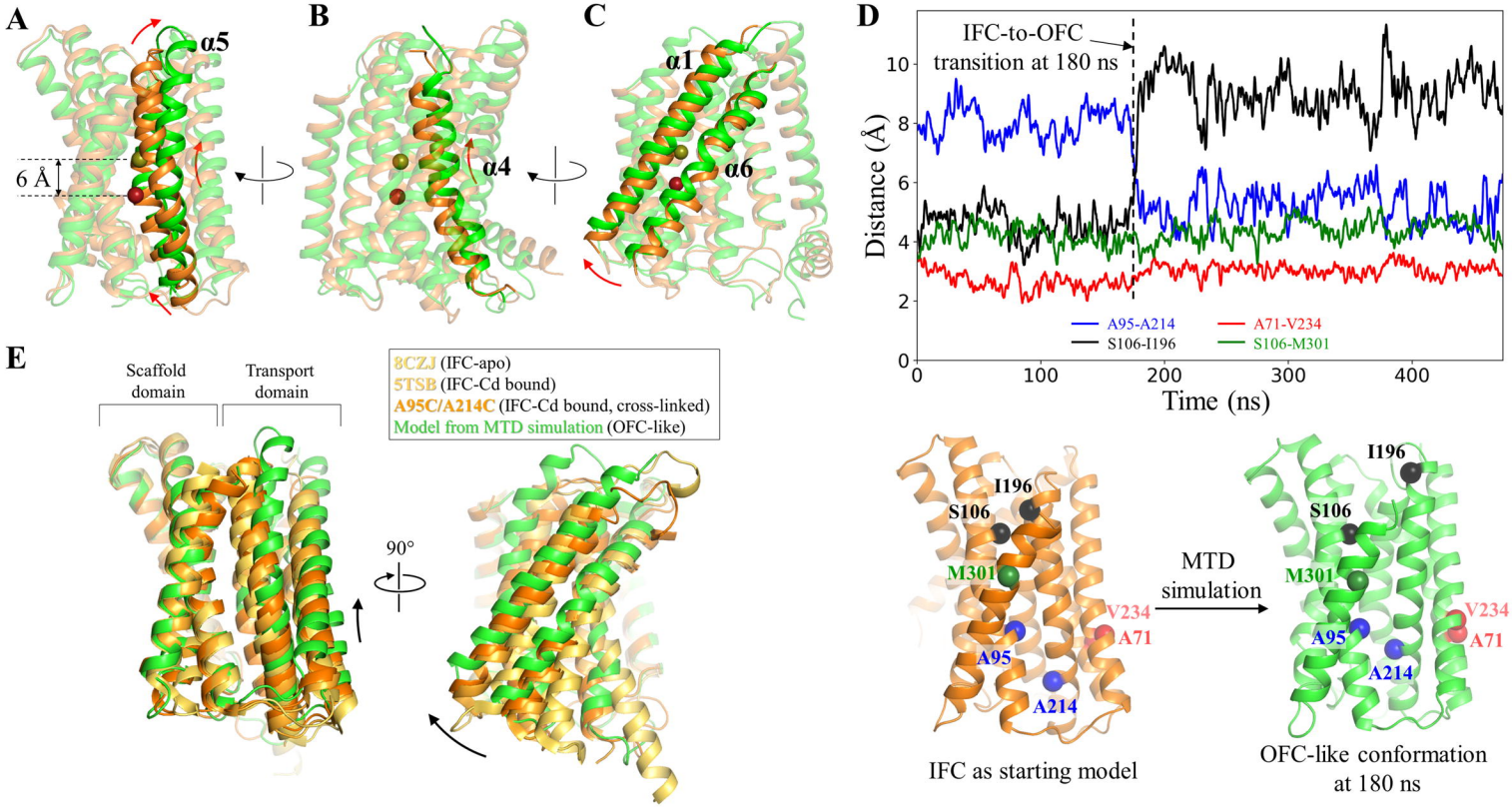
A
α5
6 Å
B
α4
C
α1
α6
D
IFC-to-OFC
transition at 180 ns
Distance (Å)
Time (ns)
A95-A214
S106-I196
A71-V234
S106-M301
E
Scaffold
domain
Transport
domain
8CZJ (IFC-apo)
5TSB (IFC-Cd bound)
A95C/A214C (IFC-Cd bound, cross-linked)
Model from MTD simulation (OFC-like)
90°
I196
S106
M301
V234
A71
A95
A214
MTD
simulation
IFC as starting model
OFC-like conformation
at 180 ns

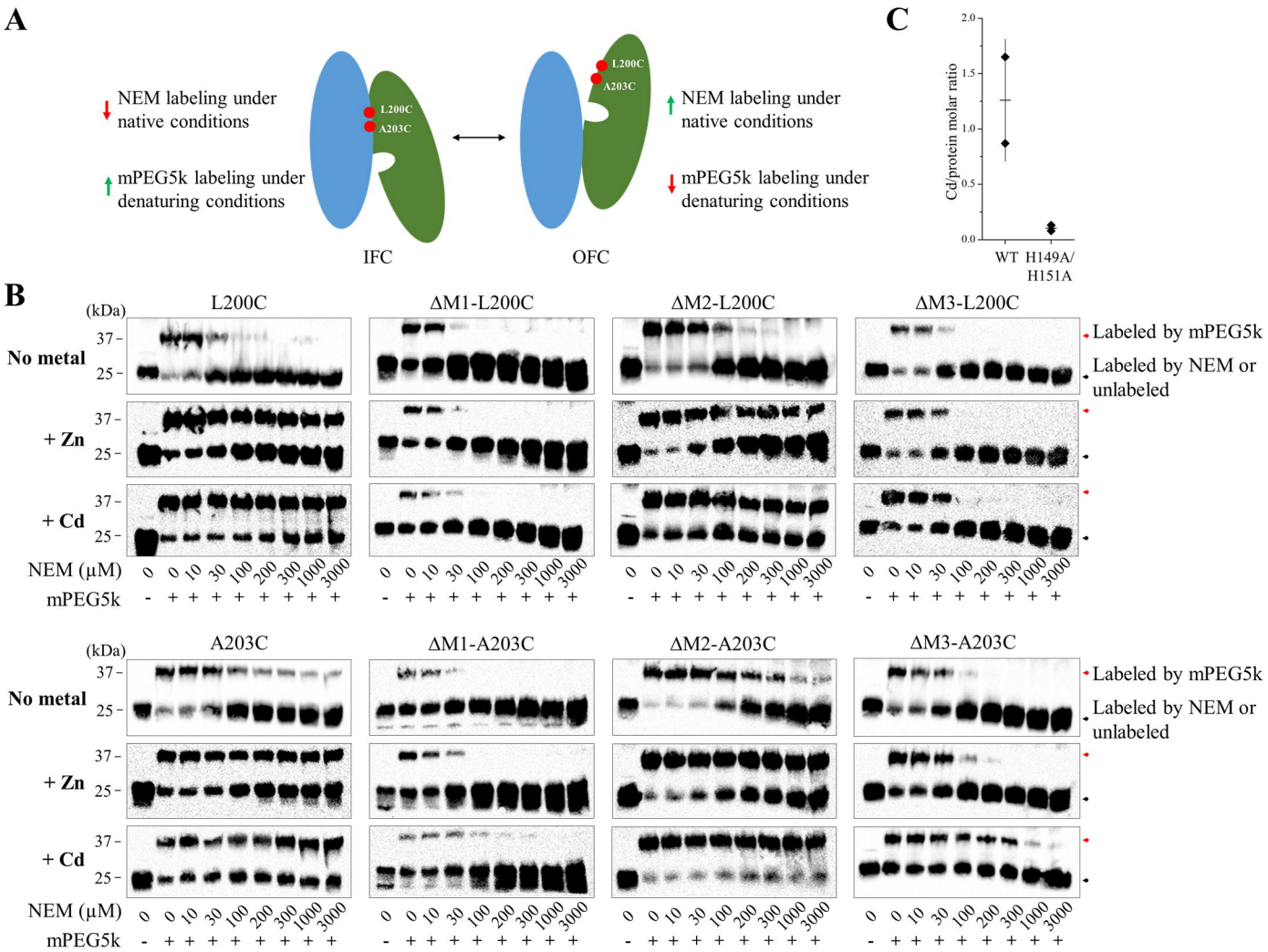
A
NEM labeling under native conditions
mPEG5k labeling under denaturing conditions
L200C
A203C
IFC
OFC
NEM labeling under native conditions
mPEG5k labeling under denaturing conditions
C
Cd/protein molar ratio
2.0
1.5
1.0
0.5
0.0
WT
H149A/ H151A
B
(kDa)
L200C
ΔM1-L200C
ΔM2-L200C
ΔM3-L200C
No metal
+ Zn
+ Cd
37
25
Labeled by mPEG5k
Labeled by NEM or unlabeled
NEM (μM)
0 0 10 30 100 200 300 1000 3000
mPEG5k
- + + + + + + + +
A203C
ΔM1-A203C
ΔM2-A203C
ΔM3-A203C

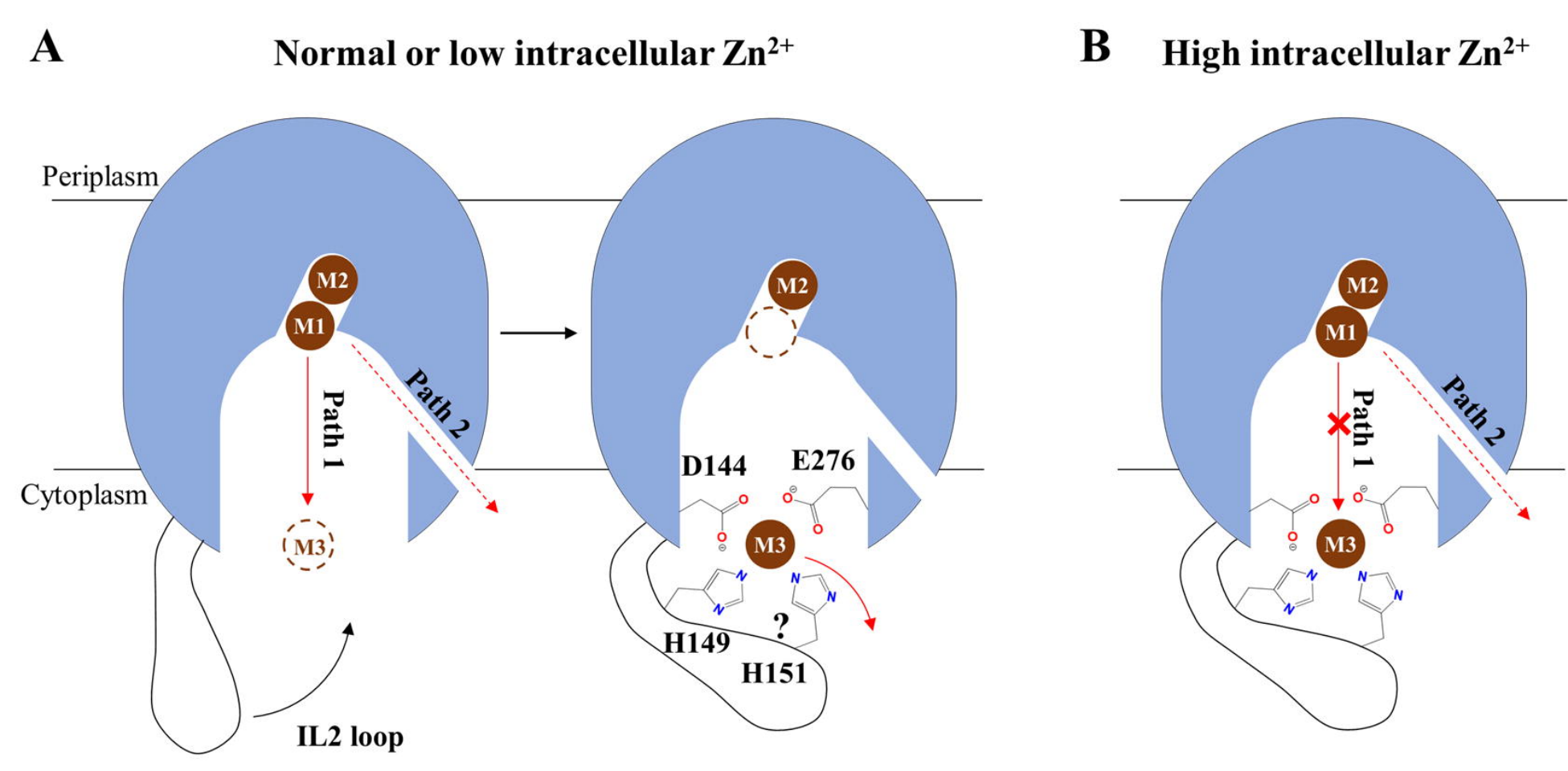
A
Normal or low intracellular Zn2+
Periplasm
Cytoplasm
M2
M1
M3
Path 1
Path 2
IL2 loop
D144
E276
H149
?
H151
B
High intracellular Zn2+

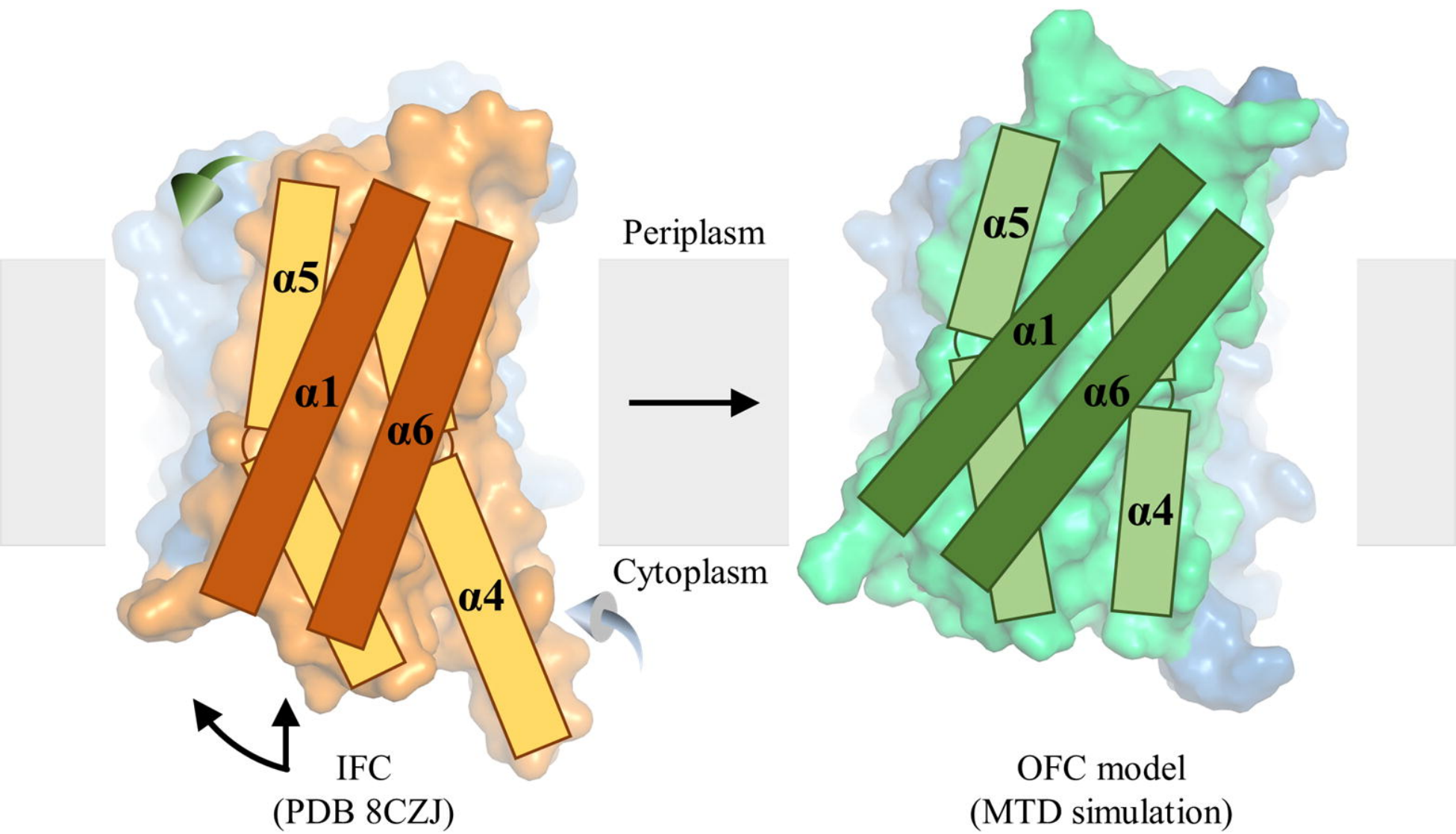
α5
α1
α6
α4
Periplasm
Cytoplasm
α5
α1
α6
α4
IFC
(PDB 8CZJ)
OFC model
(MTD simulation)